2023

RAIN-INDUCED HAZARDS IN REMOTE, LOW-RESOURCE COMMUNITIES: A CASE STUDY OF FLASH FLOODING IN THE USULUTÁN DEPARTMENT, EL SALVADOR

Natalea Cohen
Michigan Technological University, ncohen@mtu.edu

RAIN-INDUCED HAZARDS IN REMOTE, LOW-RESOURCE COMMUNITIES: A CASE STUDY OF FLASH FLOODING IN THE USULUTÁN DEPARTMENT, EL SALVADOR

By

Natalea Cohen

A THESIS

Submitted in partial fulfillment of the requirements for the degree of

MASTER OF SCIENCE

In Geology

MICHIGAN TECHNOLOGICAL UNIVERSITY

2023

This thesis has been approved in partial fulfillment of the requirements for the Degree of MASTER OF SCIENCE in Geology.

Department of Geological and Mining Engineering and Sciences

Thesis Co-Advisor:	*Luke J. Bowman*
Thesis Co-Advisor:	*John S. Gierke*
Committee Member:	*Gregory P. Waite*
Department Chair:	*Aleksey Smirnov*

Table of Contents

Acknowledgements

I would like to thank my Michigan Tech advisor Luke Bowman, co-advisor John Gierke, and committee member Greg Waite. This project would not have been possible without funding from the National Science Foundation (NSF) IRES Grant (Award No. 1855690). Thank you to Mario Hugo Méndez (Protección Civil El Salvador; delegate in the municipality of California), J. Fredy Cruz (*Universidad de El Salvador – Facultdad Mutidisciplinaria Paracentral; professor of agricultural engineering and director of graduate studies*), Nelson Aguilar (Lutheran World Relief El Salvador; assistant director), and the community members who aided my work in El Salvador. Additionally, I am grateful to the Ministry of Environment and Natural Resources (MARN) for providing precipitation data. I would like to thank David Yates, my mentor during my internship with the National Center for Atmospheric Research for his guidance with learning the Water Evaluation and Planning (WEAP) model. Finally, thank you to all my friends, family, and mentors for supporting me throughout the process.

Abstract

Rain-induced natural hazards can lead to devastating and potentially life-threatening impacts. Understanding areas susceptible to flash flooding and characterizing the intensity of flash flood events is critical in improving the mitigation and emergency preparedness of vulnerable communities. Flash floods occur on small spatial scales and for short durations making it challenging to classify flash flood susceptibility and forecast events. Modeling flash flooding becomes even more difficult when focusing on data-poor regions. This study is based in California, El Salvador, an agricultural community located in the Central American Dry Corridor (CADC), a region experiencing the impacts of climate change and associated natural hazards, including flash flood events. The research objective is to improve knowledge of rain-induced hazards in remote, low-resource communities using methods from hazard mapping and modeling. ArcGIS Pro is used to create a flash flood susceptibility map of the Usulután Department, El Salvador to gain a spatial understanding of the hazard. The Water Evaluation and Planning system (WEAP) is then applied to model sub-daily flash flooding events in a California drainage well-known for flash flooding. This study can provide insights into how an area with little surface water can still experience flash flooding, an initial step in understanding groundwater hydrology in a data-poor region. The flash flood susceptibility map created in ArcGIS Pro provides valuable information for determining potential locations of interest for flood monitoring and more in-depth analysis. The WEAP model applied field work, climate data, topography, soil infiltration rates, and other estimated variables to model flash flood events by simulating time-varying streamflow rates for various scenarios. This research seeks to promote further monitoring of rainfall and land use change, encourage increased incorporation of local knowledge to improve future flash flood research, and inspire future flash flood mapping and modeling in data-poor regions.

1 Flash Flood Susceptibility Mapping in ArcGIS Pro

1.1 Research Problem and Significance

Flash floods produced by extreme precipitation are considered one of the most deadly and destructive global natural hazards (Schumacher, 2017). While meteorological data can provide insight into rain-induced natural hazards by offering resources to map flash floods, it is challenging to accurately forecast intense rainfall events and their associated impacts. The predictability of an atmospheric phenomenon tends to decrease as the scale of motion decreases. Since extreme precipitation events occur on small spatial scales and for short durations, it is difficult to predict when a flash flood may occur (Schumacher, 2017). Predicting and mapping floods in arid regions is complicated due to a lack of hydrologic and geohydrologic data such as rainfall and runoff (Bajabaa et al., 2014). These regions suffer from the absence of data from which to base forecasting tools and understand the relationship between time-varying precipitation and land use on susceptibility to rainfall-induced hazards. Understanding the potential areas of risk to flash floods is critical in the mitigation and emergency preparedness of vulnerable communities. Furthermore, modeling flood hazard risk might serve as a basis for promoting monitoring rainfall and land use changes in the future.

California, El Salvador is an agricultural community located in the Central American Dry Corridor (CADC) (Figure 1), a region experiencing the impacts of climate change and associated natural hazards. The CADC has a length of more than 1,600 km and a width varying between 100-400 km (Gotlieb et al., 2019). It is a mountainous region that is bordered by the Pacific Coast on the west and is near the Caribbean Sea on the east. The proximity to oceans and the mountainous topography lead to highly varied weather systems and climates (Gotlieb et al., 2019). The Food and Agriculture Organization (FAO) of the United Nations reports that one of the worst droughts in the last 10 years has occurred in the CADC, particularly Guatemala, Honduras, and El Salvador (FAO, 2016). Climate forecasts conclude that when a strong El Niño phenomenon (warm phase) is weakened, it can trigger La Niña (above-normal rainfall) (FAO, 2016).

The people living within the CADC rely on subsistence farming to support the estimated 1 million families (~60% living in poverty), leading to a socially vulnerable population (Gotlieb et al., 2019). The growing number of extreme hydro-climatic events (e.g., flooding) caused by physical and social factors have increased vulnerability within at-risk populations (Hidalgo and Alfaro, 2012; Pérez-Briceño et al., 2016).

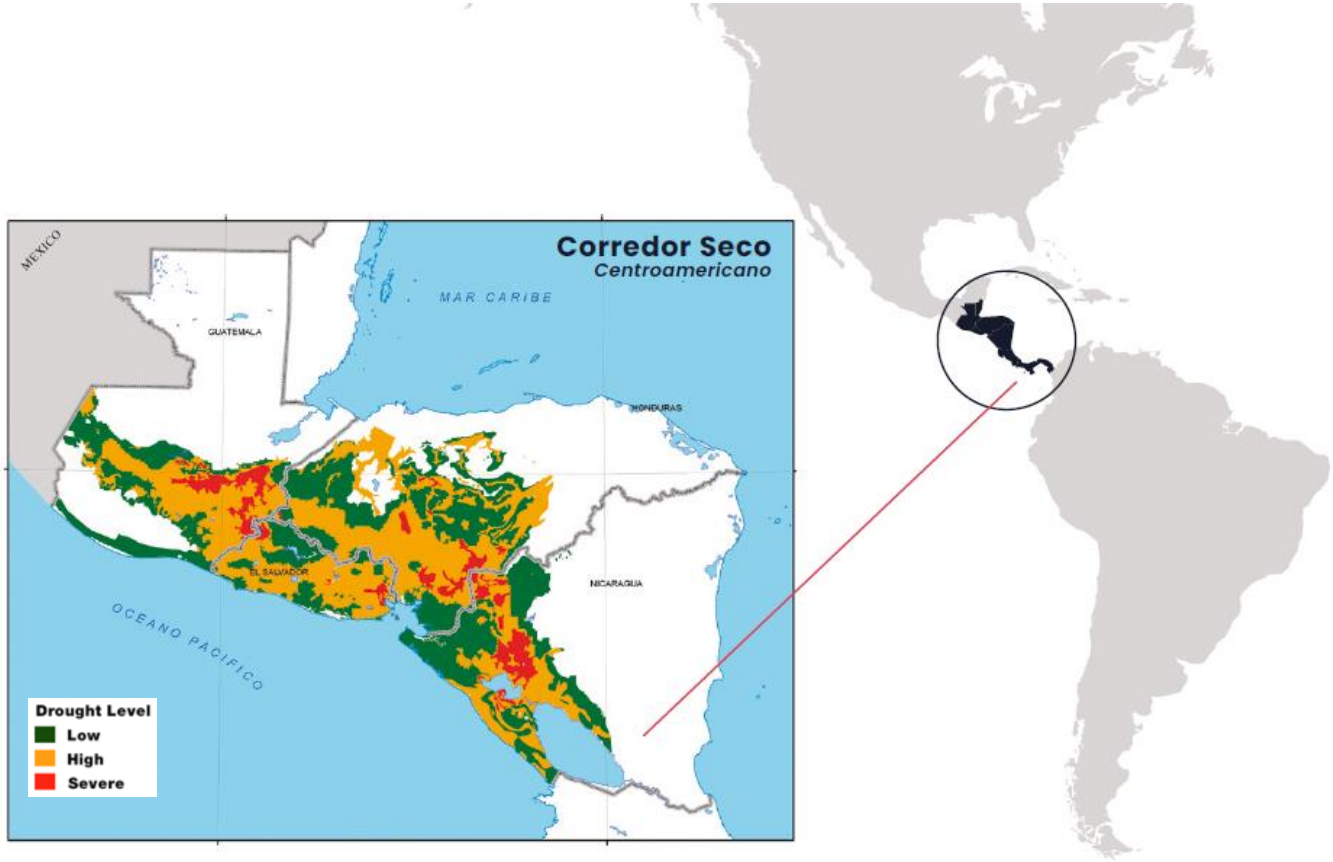

Figure 1: The Central American Dry Corridor showing grades of drought with green (low), yellow (high), and red (severe). Source: (Regional Initiative for the Dry Corridor, 2022) and (Van der Zee Arias et al., 2012).

1.2 Research Question

My research objective is to improve knowledge of susceptibility to rain-induced hazards in remote, low-resource communities using methods from hazard mapping and modeling. This study focuses on the municipality of California, El Salvador, a municipality within the Usulután Department (Figure 2). The current population of the California Municipality is over 4,000 (M Méndez 2023, personal communication, 8 March).

Michigan Technological University, the Consortium of Universities for the Advancement of Hydrologic Science Inc., and Lutheran World Relief received support from the National Science Foundation to fund the International Research Experience for Students (IRES: Award No. 1855690) program to explore agricultural community adaptations to extreme hydrometeorological events in the community of California, El Salvador. The University of El Salvador and local community stakeholders are also involved. The IRES project consists of three distinct cohorts (~10 students/cohort), each of which spends about 6 weeks in El Salvador. The first cohort occurred in 2021 and focused on characterizing the current water supply setting and assessing needs using ethnographic and social science approaches including interviews. I was a member of the Summer 2022 cohort whose work emphasized hydrology and water usage assessments based on the results from Summer 2021. The third cohort occurs in the Summer of 2023 and will continue the previous hydrologic work and likely focus on disaster risk reduction due to the interests of Lutheran World Relief. Lutheran World Relief helped identify California (Figure 3) as a research site due to the hazards the region faces related to water scarcity and climate change.

My research seeks to apply geohydrologic data related to rain-induced natural hazards to ArcGIS Pro (Esri, 2015) and the Water Evaluation and Planning system (WEAP) (Stockholm Environment Institute, 1988) in a data-poor region. The first goal of this research is to use ArcGIS Pro to map regional flash flood susceptibility of the Usulután Department, El Salvador. The second goal is to use WEAP to model sub-daily flash flooding events in a California drainage well-known for flash flooding.

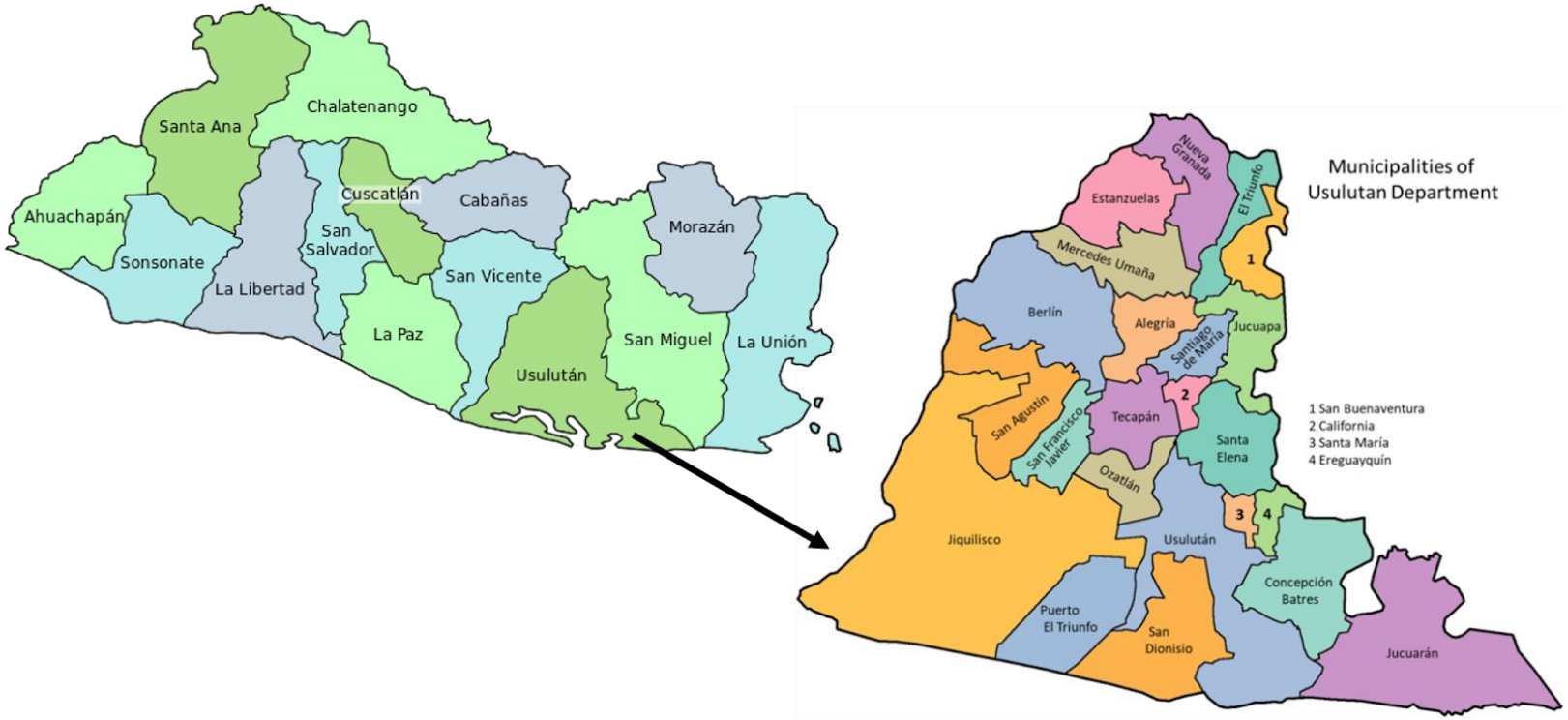

Figure 2: Map showing Departments of El Salvador and Municipalities within the Usulután Department. California Municipality is labeled with the number 2 on the Municipalities map. Source: Wikipedia (Departments of El Salvador, 2023; Usulután, El Salvador Genealogy, 2022).

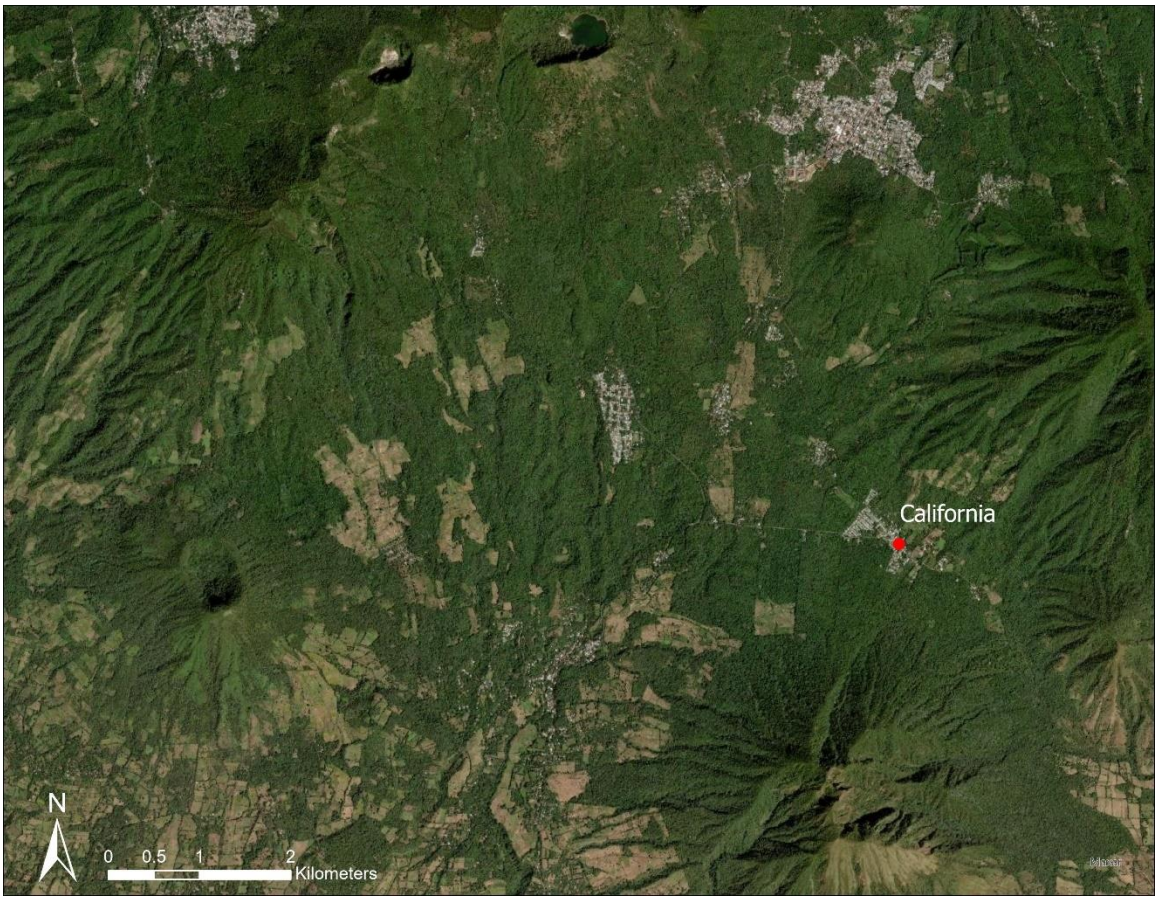

Figure 3: Map showing the community of California, El Salvador. Source: (Esri, 2015).

1.3 ArcGIS Pro Methodological Gap and Literature Review

Much work has been done to map and model flash flood hazards in areas with high-resolution digital surface models and extensive geohydrologic data available (Abdelkareem, 2017; Bajabaa et al., 2014; Curebal et al., 2016; Dawod et al., 2011; Elkhrachy, 2015; Mohamed and El-Raey, 2020; Pham et al., 2020; Youssef et al., 2011). However, little hydrologic and geohydrologic data exists in the California Municipality. As a result, mapping flood hazards in the chosen study area is difficult. The 2021 IRES cohort installed a weather station in addition to pressure transducers (measures the pressure of fluid) in local wells. The 2022 cohort installed two Arable Mark 2 instruments (collects ground-truthed data in real-time from the field on weather, soil, and crop response) and additional pressure transducers in newly identified wells. Before the IRES project, there had been no hydrometeorological data collected in the community of California leading to a large gap in data availability.

1.4 ArcGIS Pro Methods

1.4.1 Data

This study attempts to face the limitations of data availability and the lack of previous studies mapping flash floods in the Usulután Department. This is completed with ArcGIS Pro (Esri, 2015), a mapping software developed by Esri used to create, analyze, and share spatial information. Methods from a tutorial in GIS Lounge (Oppong, 2021) and MapScaping Aps (2022) are applied in ArcGIS Pro. This method maps flood susceptibility using spatial data including elevation, slope, Euclidean distance, rainfall, and land use/land cover. A flow diagram of the applied methods is shown in Figure 4.

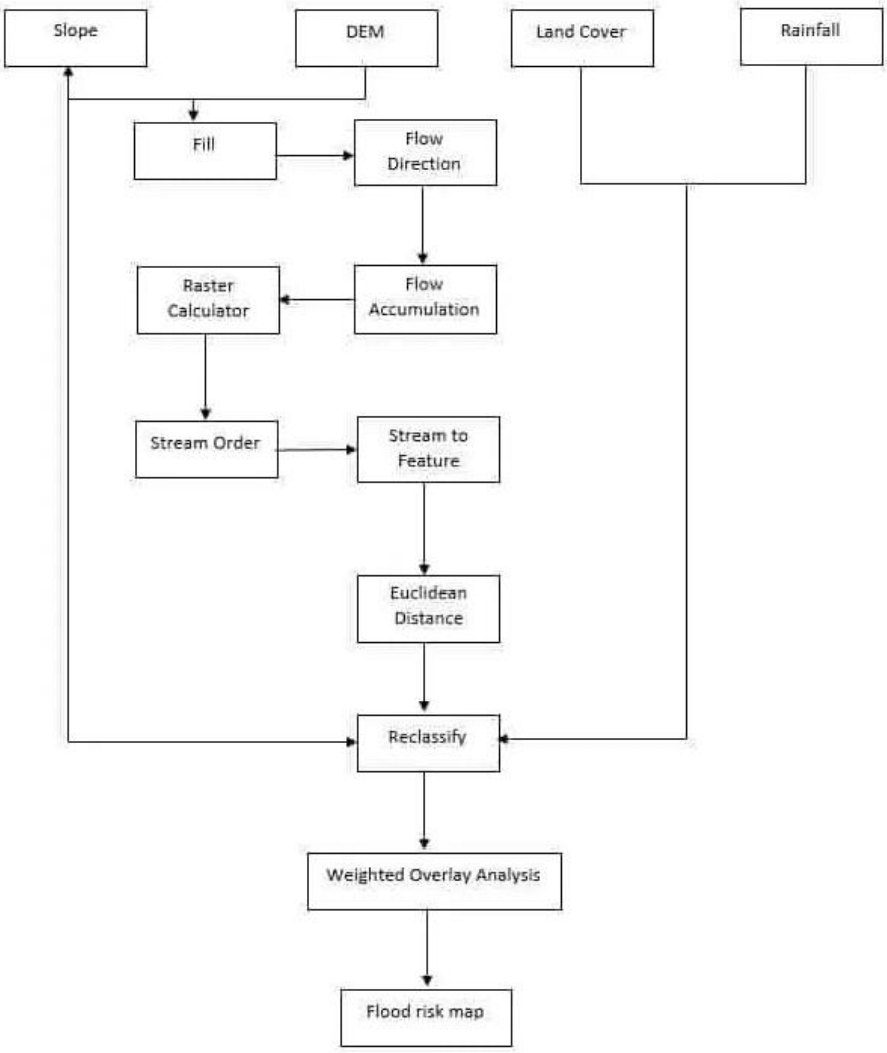

Figure 4: Flow diagram of methods used in ArcGIS Pro for flood susceptibility mapping. Source: (Oppong, 2021).

The elevation is derived directly from the 10-meter Digital Elevation Model (DEM) from 2011 (Gobierno de El Salvador). The slope is derived from the DEM using the slope tool in the Geoprocessing toolbox. The Euclidean distance is the straight-line distance from each cell to the nearest stream feature and is calculated by following the steps in the flow diagram starting at DEM (Figure 4). Land use/land cover (LULC) data is downloaded from Esri using the Sentinel-2 10m land use/land cover Timeseries Downloader (Impact Observatory, Microsoft, and Esri, 2022). The LULC includes no data, water, trees, flooded vegetation, crops, built area, bare ground, snow/ice, clouds, and rangeland.

Rainfall data is downloaded from the Center for Hydrometeorology and Remote Sensing (CHRS) at UC Irvine (CHRS, 2019). The CHRS database includes a variety of precipitation values estimated through different models. This study uses PDIR-Now because it is a real-time global 0.04x0.04-degree high-resolution dataset. Only the LULC layer from 2021 and the PDIR-Now 2021 rainfall data is used since it is the most recent data available, and this is the year when the largest range in rainfall values occurred. A large range of rainfall values is important to capture the most variance in flash flood events.

1.4.2 Reclassifying Layers

In order to use the Weighted Overlay tool, each of the five factors (elevation, slope, Euclidean distance, LULC, and rainfall) must be reclassified into the same number of defined classes using the Reclassify tool. Each layer is reclassified based on classes determined by the ArcGIS tutorial (MapScaping Aps, 2022). The 5 classes include Very Low (1), Low (2), Moderate (3), High (4), and Very High (5) flash flood susceptibility.

1.4.3 Weighted Overlay

The weighted overlay tool allows the user to assign a weight to each factor’s importance using a common measurement scale to overlay multiple raster layers (Esri, 2015). The five reclassified rasters for elevation, slope, Euclidean distance, LULC, and rainfall are added to the weighted overlay table. Under the % column, each reclassified raster's weight or influence of each parameter is assigned. The first attempt to create a base map (starting point) used the same weights as the tutorial (MapScaping Aps, 2022); elevation: 40, slope: 40, Euclidean distance: 5, land use/land cover: 5, and rainfall: 10. The sum of influences must equal 100. After running the weighted overlay tool, the final flood susceptibility map is completed.

1.4.4 Varying Weights

Selecting values to assign as weights for the weighted overlay is critical in determining plausible results of the flood susceptibility map. To explore the impacts of different weights and analyze how the results of the map change, I consulted with three Civil Protection technicians from the municipalities of California, Tecapán, and Alegría. They provided firsthand knowledge from having to manage past flash flooding events. Using Google Earth Pro, each technician separately marked and described areas that have experienced flash floods (Figure 5). Based on the 17 locations and descriptions from Civil Protection, a table is created to categorize the flood susceptibility of each location (Appendix A Table A.1). The susceptibility categories used for the ArcGIS Pro flood map are also used to classify the identified flood locations (Very High, High, Moderate, Low, and Very Low). See Appendix A Table A.1 for site names, georeferences, translated English descriptions, and classified flash flood susceptibility based on identified points by local Civil Protection technicians.

After classifying the flash flood susceptibility, these points are uploaded to ArcGIS Pro. The classified susceptibility of each point is compared to the displayed flash flood susceptibility base map (trial 1). Twelve trials to adjust the weights in ArcGIS Pro are conducted to determine which weight percentages are the most accurate, using the 17 identified flash flood locations as a guide and comparing the weight percents determined in literature related to flood modeling (Table 1) (Allafta, H. and Opp, C., 2021; Costache et al., 2019; MapScaping Aps, 2022; Pham et al., 2020; Swain, Singha, and Nayak, 2020; Yariyan, 2020; Zaharia et al., 2015).

Due to the qualitative classification of flash flood susceptibility at the 17 Civil Protection identified sites, a trial-and-error approach is used to vary the weights for elevation, slope, Euclidean distance, LULC, and rainfall for each trial. The map's displayed susceptibility for each location is compared to the Civil Protection classified susceptibility resulting in a match % for each trial. The nature of qualitative classification is challenging because the identification of high, moderate, and low susceptibility may vary between each of the three Civil Protection technicians. Additionally, some technicians oversee areas with more pavement (likely increased flash flooding), compared to areas without pavement (potentially less flash flooding).

The first trial results in a susceptibility map using the same weights as the tutorial (MapScaping Aps, 2022); elevation: 40, slope: 40, Euclidean distance: 5, land use/land cover: 5, and rainfall: 10. Trial 1 is considered the starting point from which to adjust weights and better match the map's displayed susceptibility to the classified susceptibility. Trial 1 results in a 52.94% match between classified and displayed susceptibility. The best-fit map occurs with Trial 12 (58.82% match) by adjusting weights as follows; elevation: 40, slope: 40, Euclidean distance: 5, land use/land cover: 10, and rainfall: 5 (Figure 6).

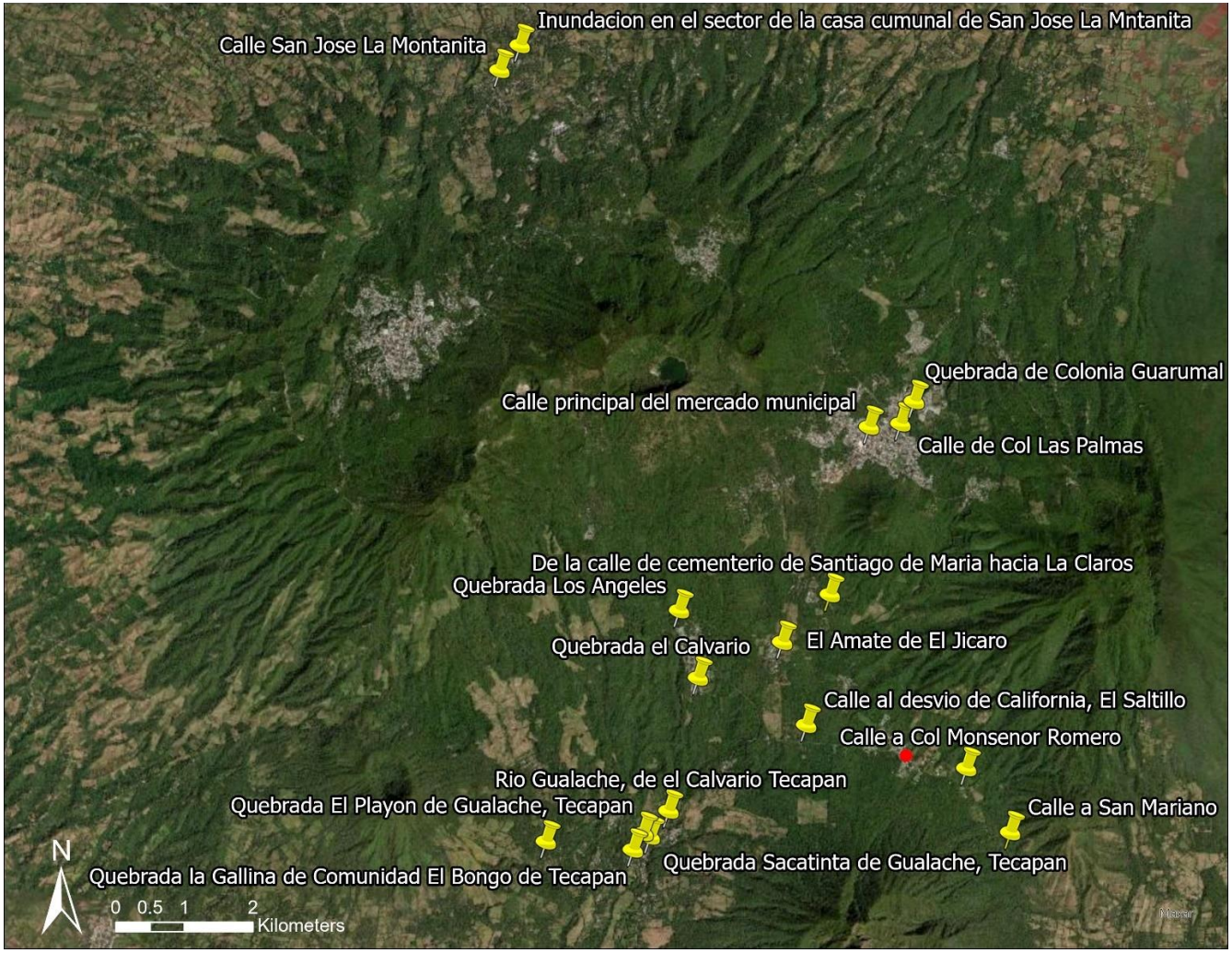

Figure 5: Susceptible flash flood locations identified by local Civil Protection technicians. Source: (Esri, 2015).

Table 1: Flash flood susceptibility (High, Moderate/"Mod.", Low) values at identified locations by Civil Protection for varied weights in ArcGIS Pro.

Name	Classified Suscep.	Trial 1	Trial 2	Trial 3	Trial 4	Trial 5	Trial 6	Trial 7	Trial 8	Trial 9	Trial 10	Trial 11	Trial 12
Raster: Weight		DEM:40 Slope:40 Euclid:5 LULC:5 Rain:10	DEM:35 Slope:35 Euclid:8 LULC:8 Rain:14	DEM:30 Slope:40 Euclid:15 LULC:5 Rain:10	DEM:25 Slope:40 Euclid:20 LULC:5 Rain:10	DEM:25 Slope:35 Euclid:30 LULC:5 Rain:5	DEM:40 Slope:35 Euclid:15 LULC:5 Rain:5	DEM:35 Slope:35 Euclid:15 LULC:5 Rain:10	DEM:35 Slope:40 Euclid:15 LULC:5 Rain:5	DEM:40 Slope:40 Euclid:10 LULC:5 Rain:5	DEM:35 Slope:35 Euclid:10 LULC:10 Rain:10	DEM:35 Slope:40 Euclid:5 LULC:15 Rain:5	DEM:40 Slope:40 Euclid:5 LULC:10 Rain:5
% Match with Classified Susceptibility		52.94%	52.94%	47.06%	41.18%	35.29%	47.06%	47.06%	47.06%	47.06%	47.06%	52.94%	58.82%
Calle a Col Monseñor Romero	High	Mod.	Mod.	High	High	High	Mod.	Mod.	High	Mod.	Mod.	High	Mod.
De la calle de cementerio de Santiago de María hacia La Claros	High	Mod.	Mod.	Mod.	High	High	Mod.	Mod.	Mod.	Mod.	Mod.	Mod.	Mod.
Calle a San Mariano	High	High	High	High	High	High	High	High	High	High	High	High	High
Calle al desvío de California, El Saltillo	High	High	High	High	High	High	Mod.	Mod.	High	Mod.	Mod.	High	High
Quebrada el Calvario	Mod.	Mod.	Mod.	Mod.	Mod.	High	Mod.	Mod.	Mod.	Mod.	Mod.	Mod.	Mod.
El Amate de El Jícaro	Mod.	Mod.	Mod.	High	High	High	Mod.	Mod.	High	Mod.	Mod.	High	Mod.
Quebrada Los Angeles	Mod.	Mod.	Mod.	Mod.	High	High	Mod.	Mod.	Mod.	Mod.	Mod.	Mod.	Mod.
Rio Gualache, del Calvario Tecapán	Low	High	High	High	High	High	High	High	High	High	High	High	High
Quebrada Sacatinta de Gualache, Tecapán	Low	High	High	High	High	High	High	High	High	High	High	High	High
Quebrada El Playón de Gualache, Tecapán	Low	High	High	High	High	High	High	High	High	High	High	High	High
Quebrada la Gallina de Comunidad El Bongo de Tecapán	Mod.	Mod.	Mod.	Mod.	High	High	Mod.	Mod.	Mod.	Mod.	Mod.	Mod.	Mod.
Quebrada de Arena de Loma Pacha de Los Chapetones, Tecapán	Low	Mod.	Mod.	High	High	High	High	High	High	High	Mod.	Mod.	Mod.
Calle San José La Montanita	High	High	High	High	High	High	High	High	High	High	High	High	High
inundación en el sector de la casa comunal de San José La Montanita	High	High	High	High	High	High	High	High	High	High	High	High	High
Calle principal del mercado municipal	Mod.	High	High	High	High	High	High	High	High	High	High	High	High
Calle de Col Las Palmas	Mod.	Mod.	Mod.	High	High	High	Mod.	Mod.	High	Mod.	Mod.	High	Mod.
Quebrada de Colonia Guarumal	Mod.	High	High	High	High	High	High	High	High	High	High	Mod.	Mod.

1.5 ArcGIS Pro Results

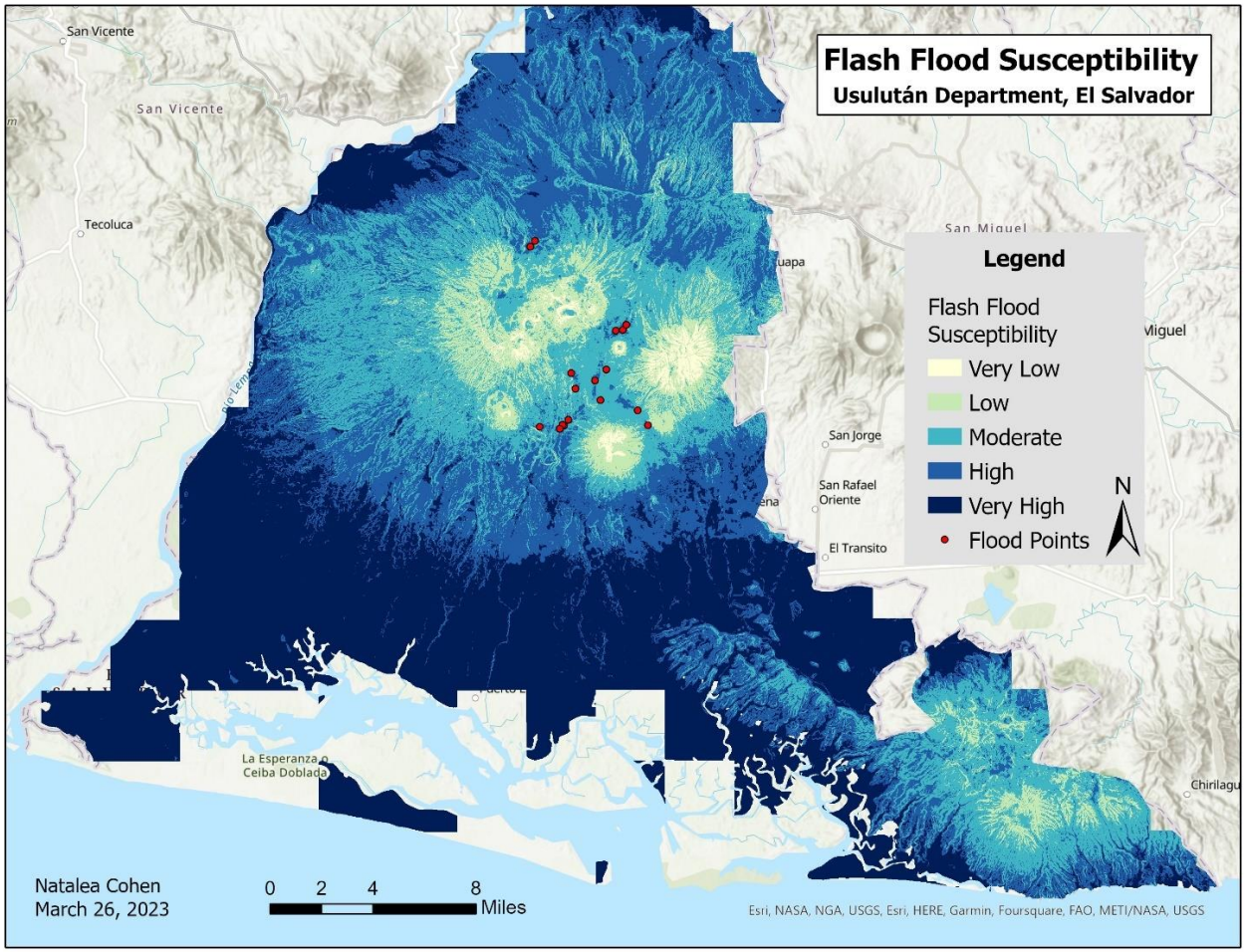

Figure 6: Best-fit flash flood susceptibility map of Usulután Department, El Salvador. Source: (Esri, 2015).

1.6 ArcGIS Pro Discussion

The best-fit flash flood susceptibility map of the Usulután Department, El Salvador displays flash flood susceptibility ranging from very low to very high (Figure 6). The best-fit map weights included elevation: 40%, slope: 40%, Euclidean distance: 5%, land use/land cover: 10%, and rainfall: 5%. The map results are compared with the reclassified raster layers for each factor. The results are highly dependent on elevation and slope due to the prominent weight percentages (40%) which is apparent in the final flash flood map. Areas displayed as very low and low susceptibility zones are located at higher elevations (volcanic peaks and slopes) and susceptibility decreases as elevation and slope decreases. The moderate and high flash flood susceptibility is shown in areas at low elevations and slopes (base of volcanoes and plains). Very high susceptibility occurs towards the coast.

It is difficult to discern the relationship between the Euclidean distance and susceptibility zones as the study area is classified by the same Euclidean distance range (0-618.699) and only weighted at 5%. For LULC (10% weight), very low, low, and moderate flood susceptibility tends to occur in areas heavily dominated by trees with some rangeland/crops and water/built area/flooded vegetation. Areas with high and very high flood susceptibility occur in areas dominated by rangeland/crops and water/built area/flooded vegetation with some trees. There are some areas near the coast on the south end of the flood map that do not show up in the map (Figure 6). This is likely due to a lack of rainfall data in this area. It can be assumed that the missing area would likely be displayed as very high susceptibility due to the flood susceptibility around the missing area being very high. If this were the case, the missing area (very high flash flood susceptibility) would theoretically occur in space dominated by water/built area/flooded vegetation with some trees and rangeland/crops. There are no clouds/snow/ice or bare ground causing these classes to have no impact on the resulting flash flood map. Rainfall had a 5% weight and in general, the highest amount of rainfall occurred in the north section of Usulután and rainfall amount generally decreased moving south. The impact of rainfall on the final flash flood susceptibility map can be particularly observed in the north section of the map where the rainfall was the highest. This likely contributed to map results in the north being dominated by high and moderate with some very high flash flood susceptibility. Future work would include assigning larger weight percentages to Euclidean distance, LULC, and rainfall to analyze the model sensitivity for those factors.

Overall, despite varying weight percentages, the map tends to overestimate flash flood susceptibility (Table 1). The best match percentages occur when the DEM and slope are set to combinations of 35 and 40, Euclidean distance ranges from 5-8, LULC ranges from 5-15, and rainfall ranges from 5-14. Note that it was not possible to match all 17 points to the exact classified susceptibility, however, the displayed susceptibilities were improved to better represent the classified susceptibilities. The match percentage does not improve past 58.82% largely since three of the 17 identified locations (Río Gualache, De el Calvario Tecapán; Quebrada Sacatinta de Gualache, Tecapán; and Quebrada El Playón de Gualache, Tecapán) are classified as low susceptibility, but

displayed as high in all 12 trials despite adjusting the weights. Civil Protection described these areas as flooding when tropical storms pass 70 mm of precipitation. As a result, these three areas are classified as Low. ArcGIS Pro likely displayed them as High flash flood susceptibility since they are in areas at low elevations and with low slopes, and both elevation (40%) and slope (40%) have a large influence on the resulting map.

This flash flood susceptibility map provides a regional approximation of flash flood susceptibility and aids in identifying regions of interest. It led me to identify areas of interest that could be looked at with greater spatial resolution and gave me a starting point/reference for my discussion to confirm flood locations with Civil Protection and their areas of interest. The map also provided an initial understanding of the hydrology of the region to support the next phase of my work with the National Center for Atmospheric Research (NCAR) and the Water Evaluation and Planning system (WEAP).

2 Flash Flood Modeling in WEAP

2.1 WEAP Methodological Gap and Literature Review

During the spring 2023 semester of my masters (December 2022-April 2023) I was selected to work with the National Center for Atmospheric Research (NCAR) as a fellow through the Advanced Study Graduate Visitor Program. During the fellowship I was mentored by Dr. David Yates, a scientist in the Research Applications Lab Hydrometeorological Applications Program at NCAR in Boulder, Colorado. Dr. Yates taught me how to use the Water Evaluation and Planning system (WEAP) (Stockholm Environment Institute, 1988) in a unique and valuable manner. The WEAP model is a software tool with the traditional application being to model scenarios related to water resource planning using an integrated approach (Stockholm Environment Institute, 2023). Features of WEAP are listed in Table 2. For this study, the WEAP system is applied in a novel way to model flash floods in watersheds within the municipal region of California, El Salvador (Figure 7).

Table 2: Features of WEAP software. Source: (Stockholm Environment Institute, 2023).

WEAP Highlights

Integrated Approach	Unique approach for conducting integrated water resources planning assessments
Stakeholder Process	Transparent structure facilitates engagement of diverse stakeholders in an open process
Water Balance	A database maintains water demand and supply information to drive mass balance model on a link-node architecture
Simulation Based	Calculates water demand, supply, runoff, infiltration, crop requirements, flows, and storage, and pollution generation, treatment, discharge and instream water quality under varying hydrologic and policy scenarios
Policy Scenarios	Evaluates a full range of water development and management options, and takes account of multiple and competing uses of water systems
User-friendly Interface	Graphical drag-and-drop GIS-based interface with flexible model output as maps, charts and tables
Model Integration	Dynamic links to other models and software, such as QUAL2K, MODFLOW, MODPATH, PEST, Excel and GAMS

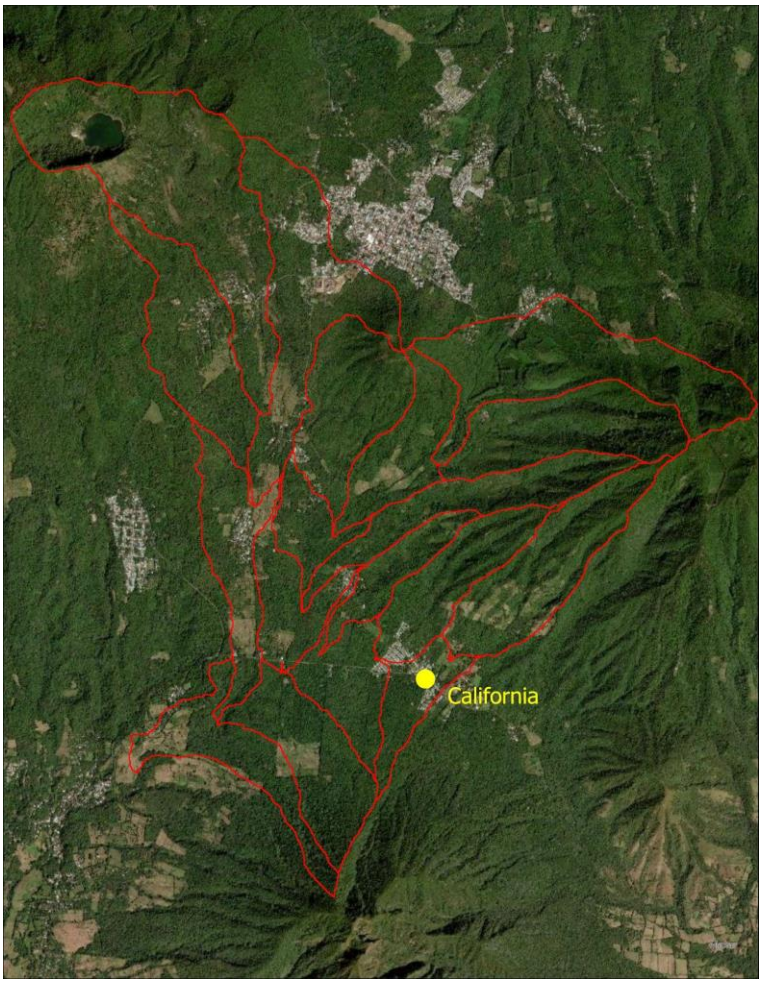

Figure 7: Map of watersheds identified for WEAP analysis.

WEAP was developed in 1988 and has been used primarily to model water resource management scenarios in large cities with a nearby surface water source. Unlike past studies, this new application of WEAP aims to model flash flood hazards at the local scale in an area with little surface water expression and very limited data availability. The first significant application of WEAP was in 1989 and explored water demand and supply simulations for 1987-1989 and forecasting to 2020, considering continuous practices at the time (Raskin et al., 1992). Since 1989, there have been various applications of WEAP, mostly related to water resource management (Agarwal et al., 2019; Hadded et al., 2013; Hamlat et al., 2013; Höllermann et al., 2010; Lévite et al., 2003; Li et al., 2015; Mounir et al., 2011). Sieber and Purkey (2015) published a WEAP User Guide that provides an in-depth technical description of WEAP. The Stockholm Environment Institute created a WEAP tutorial composed of stand-alone modules to aid in learning the WEAP software. There are very limited flood applications previously performed by WEAP (Foroodi et al., 2021; Moein, 2013).

Over the years, WEAP features have grown, and it has been used in novel applications that have improved the original intentions of WEAP. The Long-range Energy Alternatives Planning System (LEAP) is a Stockholm Environment Institute software tool used for energy policy analysis and climate change mitigation assessment (Stockholm Environment Institute, 2023). Due to growing concern regarding the environmental impact of energy systems, there have been an increased number of recent studies linking LEAP with WEAP (Fard and Sarjoughian, 2020; Hamed, 2020; Liu et al., 2021). Additionally, WEAP has been increasingly used for modeling effects of water pollution (Kavand et al., 2020; Shakak, 2022). The Stockholm Environment Institute recently introduced the WASH Flows analytical tool designed to link watershed management and water, sanitation, and hygiene (Claure, 2023). The WASH Flows tool can also be coupled with watershed-scale models including WEAP (Stockholm Environment Institute, 2023).

While WEAP has been mainly used for water resource planning studies in the past, it has the potential for other valuable applications, including flash flood modeling. Flash flood modeling requires high spatial- and temporal-resolution considerations. There are other flood modeling methods such as the Analytical Hierarchy Process (AHP) which is based on multi-criteria decision-making (Costache et al., 2019). However, most flood models tend to be more complex, are more time-consuming, and require extensive data (Costache et al., 2019). The WEAP model is not necessarily the best or most accurate method for flash flood modeling, however, it does provide the user with a less time-consuming model that requires minimal data to run; an important characteristic when trying to overcome the challenges of a data-poor setting.

California, El Salvador is in a region with almost no perennial surface water and consists of a small agricultural community with little water resource availability. It is surrounded by highly vegetated, dormant volcanoes and the land use is predominantly coffee plantations. This community is currently facing the harsh impacts of climate change-induced natural hazards including flash floods and the local Civil Protection does

not currently keep a record of flash flood events that have occurred in the past, though they are frequent. This study aims to apply WEAP in a manner that has not been attempted before, which is modeling sub-daily flash flooding events at the local, small community-sized scale.

2.2 WEAP Methods

Hydrological modeling with WEAP, at its basic level, requires climate data for characterizing rainfall and evapotranspiration, topography to delineate watershed boundaries and drainages, and soil infiltration rates. The model estimates will reflect hydrology in relation to the quality of the data available for these basic components. In addition to the above-mentioned factors, WEAP requires other variables such as runoff resistance factor, travel time, diffusion, and other factors which are estimated based on available data and knowledge of the environment. After inputting the necessary variables and running the model, WEAP can simulate flash flood events by determining streamflow rate given the assigned values for each contributing variable.

2.2.1 Rainfall Data

Prior to August 2021, no meteorological data existed for the community of California. The closest weather station to California with accessible data was located 4.3 km away in Santiago de María and managed by the Ministry of Natural Resources and the Environment (MARN). The MARN precipitation data consists of daily data, which was not applicable for this study since we are modeling sub-daily and even sub-hourly flash flood events. Rainfall data in the California community is currently collected with the Vantage Pro2™ Davis Instrument (Vantage Pro2™, 2023) weather station which was installed on August 10, 2021 (Figure 8). Data is collected at 15-minute intervals and the station measures precipitation, air temperature, relative humidity, solar radiance, wind speed and direction, and barometric pressure. The 15-minute Davis precipitation data is converted to daily data to compare with the MARN rainfall data from Santiago de María from April 1, 2022 - November 27, 2022 (Figure 9). Generally, heavy precipitation events show consistency between both locations, however, there are times when Santiago de María experienced notably more rainfall than California and vice versa (July 22, 2022).

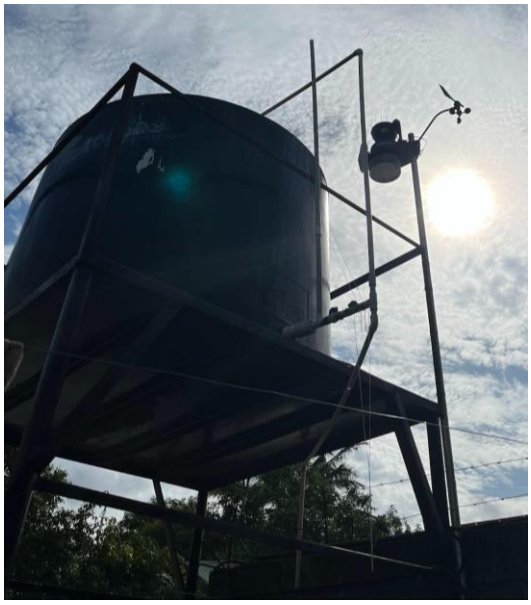

Figure 8: Installed Vantage Pro2™ weather station.

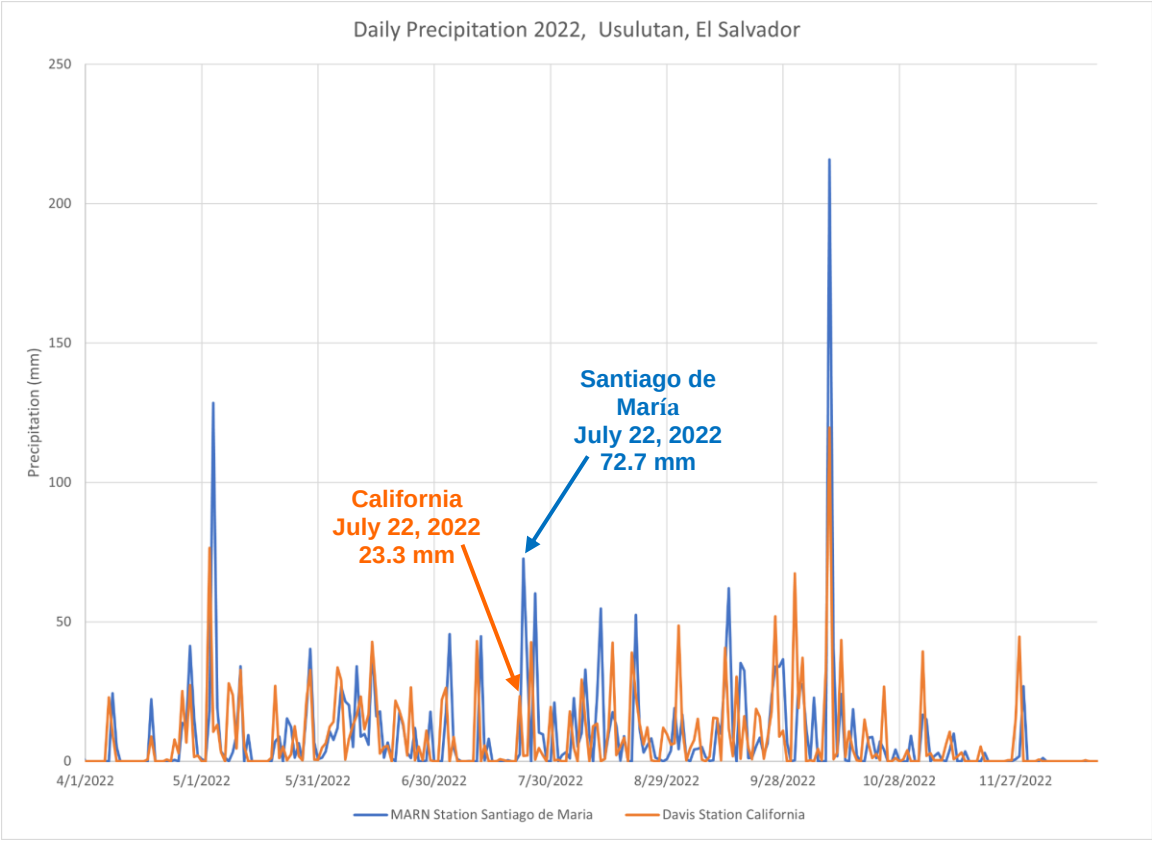

Figure 9: Santiago de María (MARN) and California (Davis) daily rainfall comparison for 2022.

Timesteps in WEAP are only as short as a day and typically used to analyze daily data. Flash floods occur over shorter intervals, so the approach to account for time in WEAP was modified to match our 15-minute rainfall data. Years in WEAP were treated, instead, as numbered days, which appeared like 4-digit years. The timestep is adapted to the 15-min data by creating 96 timesteps (96 15-min intervals in one day) per “numbered day” (considered as a year) in WEAP. The Current Accounts represents the first day and the scenarios are subsequent days. The first day of the simulation (8/11/21) was assigned the "year" 1901. Day 2 would then be 1902. The final day of the simulation period (2/14/23) was then WEAP "year" 2453. Where precipitation data is missing likely due to power outages, the number -999 is input as a filler. Only the Year, Timestep, and Precipitation columns in the .csv file are needed to import into WEAP. The Excel file containing the rainfall data can be found in the supplemental materials. The Vantage Pro2™ weather station data shows that total rainfall for a full rainy season which ranges from 4/7/22 (2140 in WEAP) - 11/28/22 (2375 in WEAP) is 2184.5 mm (2.1845 m). Day-based variables and parameters that WEAP uses were adjusted by dividing by 96 to reflect the variable or parameter on a per timestep basis, timesteps being 15 minutes.

2.2.2 Flash Flooding in La Claros

La Claros is a community located 2-km northwest of California. During fieldwork in California March 6-10, 2023, I had the opportunity to speak with residents about flash flooding in the area. They confirmed that the road from Santiago de María to California (Calle Vieja/Old Road) is highly susceptible to flash flooding during heavy precipitation and that water flows down Old Road from Santiago de María (city 2.3-km north of La Claros), past La Claros, and then abruptly turns southwest into a drainage, instead of continuing down Old Road (the drainage is incised more deeply and the road increases slightly in elevation away from the drainage). A video taken by a local from La Claros on July 22, 2022, displays an example of flash flooding along Old Road (Figure 10). I drove Old Road starting from La Claros to Santiago de María and noted erosion caused by flash flooding (Figure 11). Residents spoke of flooding that was about 1-m deep as frequently as ten times during a rainy season, although they have no formalized record of observational data to quantify the frequency, duration, nor extent of flooding.

The drainage begins 0.4-km southeast of La Claros. The first 50-m downslope of the drainage is a narrow rectangular channel roughly 2-m wide and 1-meter deep (Figure 12). Another 60-70-m downslope, the channel begins forming a rocky shallow U-shape measuring roughly 6-m wide and 3-m deep (Figure 13). Further downslope (1-km), the wide U-shaped channel reverts to the narrower 2-m wide, 1-m deep rectangular-like channel. After following the drainage almost 2-km southwest, it is constricted by a ~1.2-m diameter culvert located under the main road that goes from road RN14 to California (Figure 14). The road above the culvert is flooded during heavy precipitation events, not because the culvert is insufficient to handle the flow, but because overland flow from the main road into/out of California accumulates in this drainage. The drive from Santiago de María to the La Claros drainage and the drainage path were recorded using onX Hunt: GPS Hunting Maps phone app (onXmaps, Inc., 2023). Figure 15 displays the path and

elevation profile of Old Road and Figure 16 shows the La Claros drainage path and elevation profile in Google Earth. Georeferenced images taken during the La Claros drainage walk are uploaded to Google Earth and named DW1-17 (Figure 17). These images were used to estimate the La Claros drainage width and height at different locations. See Appendix B Table B.1 for the Google Earth images georeferenced, estimated channel dimensions, and estimated bankfull flow using Manning's equation.

Figure 10: Old Road flash flood from July 22, 2022.
Video taken by La Claros community member.

Figure 11: Old Road damage caused by past flash flood events.

Figure 12: Beginning of La Claros drainage walk where the channel is narrower (2-m wide and 1-meter deep).

Figure 13: Rocky u-shaped section of La Claros drainage (6-m wide and 3-m deep).

Figure 14: Culvert at the end of the La Claros drainage where water overflows and floods the road above.

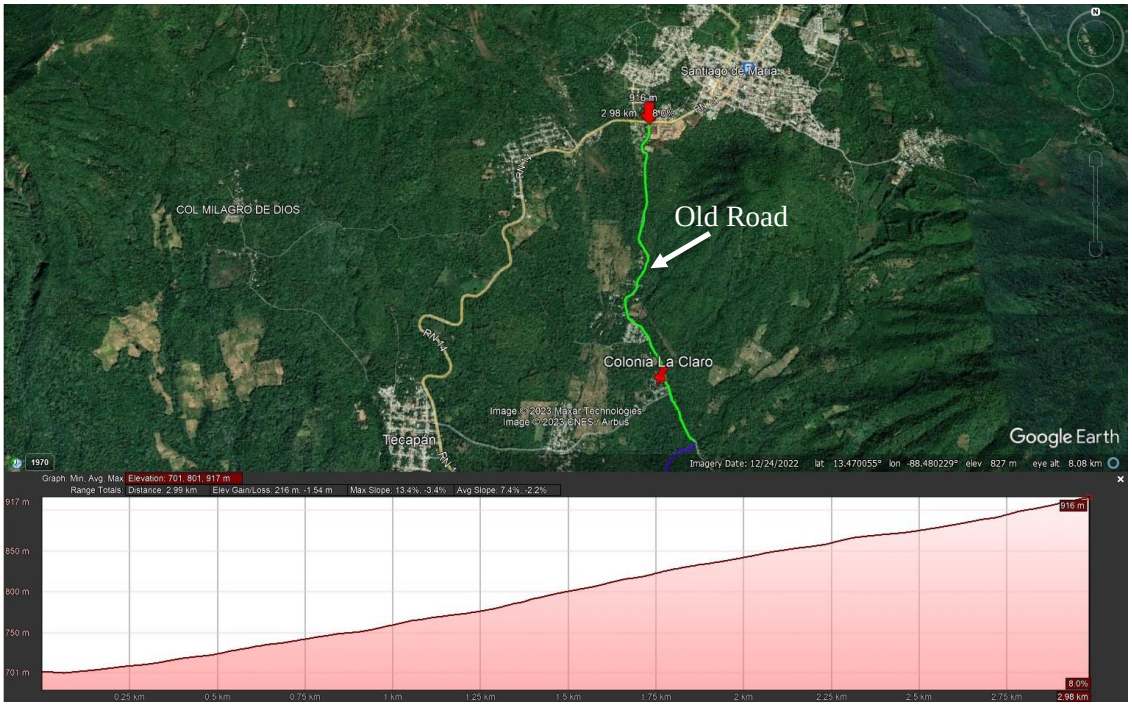

Figure 15: Left-to-right in profile view, south to north (green line). Drive from La Claros drainage (703 m) to Santiago de María (916 m) and elevation profile in Google Earth.

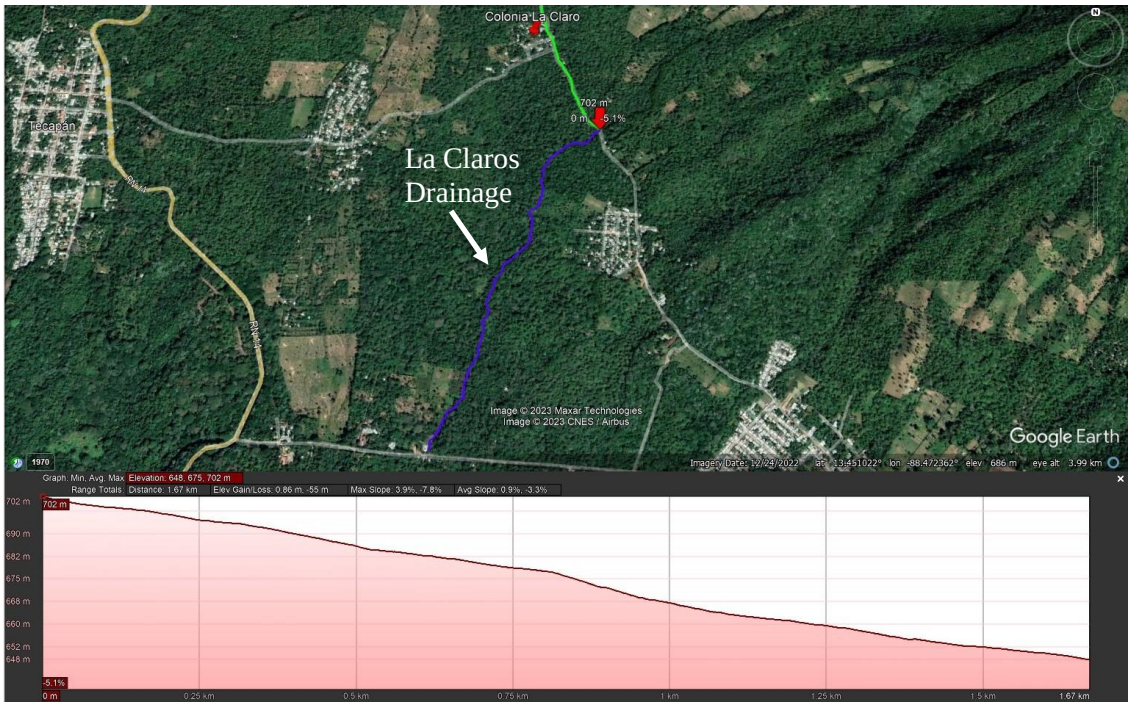

Figure 16: Left-to-right in profile view, NNE-SSW (blue line). Walk from start of La Claros drainage (703 m) to end of drainage (648 m) and elevation profile in Google Earth.

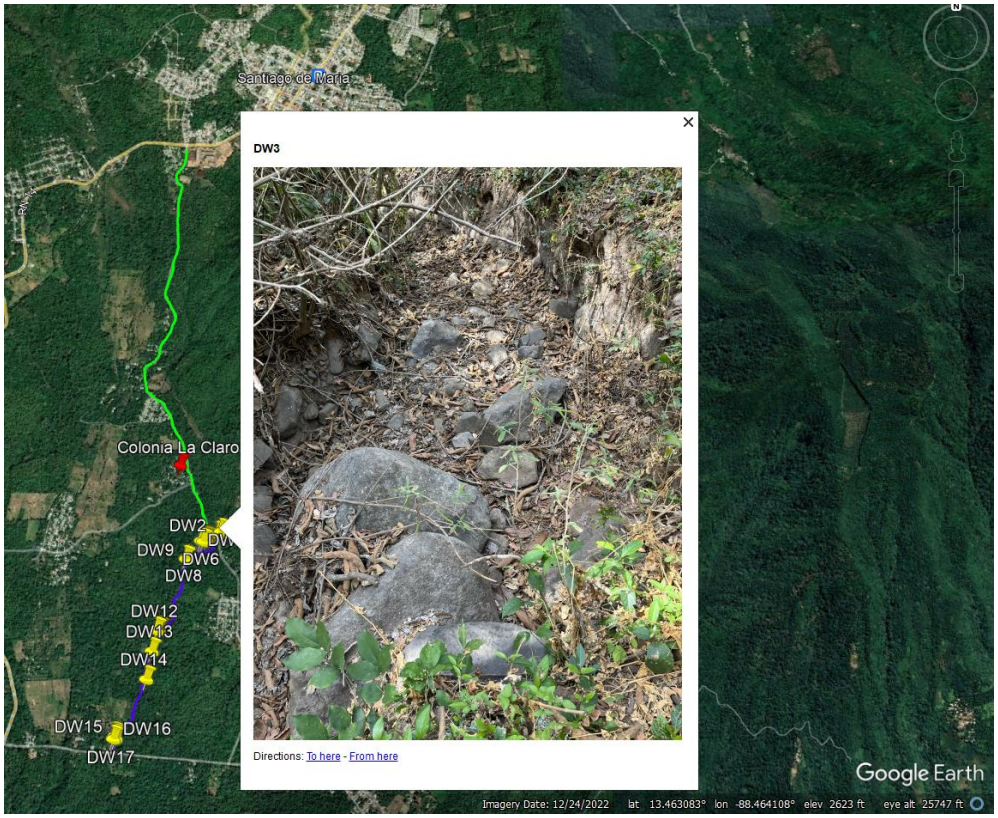

Figure 17: Google Earth imported georeferenced image locations of La Claros drainage walk.

2.2.3 Infiltrometer Tests

2.2.3a Infiltrometer Background

Another input to improve the accuracy of the flood model in WEAP is saturated hydraulic conductivity (K_{sat}) of the surficial soil deposits. In this study, K_{sat} is used to help define the soil structure for flash flood inputs in the WEAP model.

There are various methods to calculate and measure K_{sat}. Since we were interested in K_{sat} for the purposes of estimating infiltration rates, we used an infiltrometer to collect data and the Glover solution to analyze the data:

$$K_{sat} = \frac{Q}{2\pi H^2}\left[\sinh^{-1}\left(\frac{H}{r}\right) - \left\{\left(\frac{r}{H}\right)^2 + 1\right\}^{\frac{1}{2}} + \frac{r}{H}\right]$$

Equation (1)

Equation (1) is the Glover solution for calculating the saturated hydraulic conductivity (K_{sat}) in surficial (i.e., uppermost meter) deposits from constant head infiltrometer data. K_{sat} is measured using the steady-state rate of water flow (Q) from a cylindrical auger hole of known diameter (2r) under a constant head of water (H) (Amoozegar, 2002).

The Glover solution considers only the saturated flow that occurs around the auger hole (Zangar, 1953). In this study, the Perm-It™ constant-head infiltrometer (Figure 18) is used to gather field measurements at three sites named LL, LC, and BH (Figure 19) along the road from Santiago de María to the La Claros drainage, both of which are highly susceptible to flash flooding (Figure 20). A cross-sectional view of the soil being tested is shown in Figure 21.

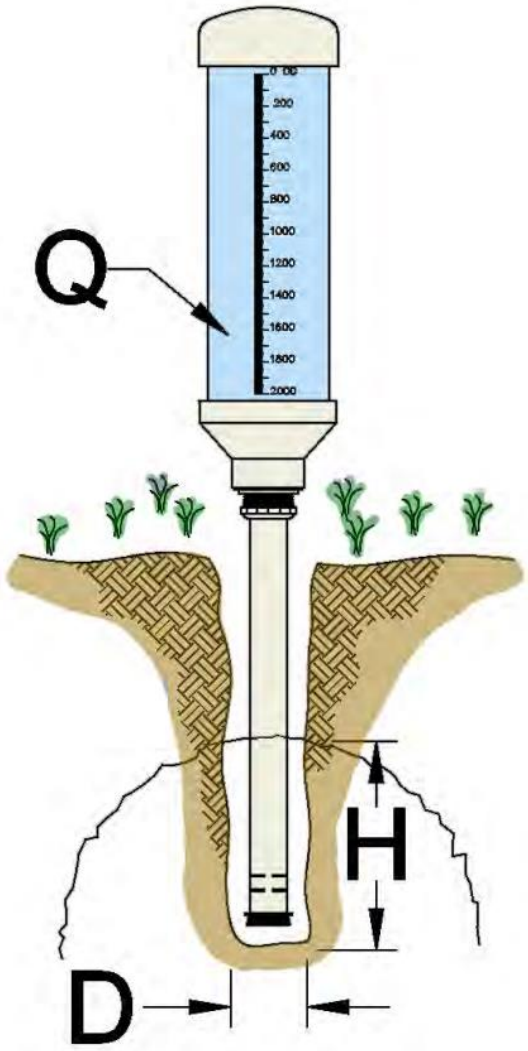

Figure 18: Schematic illustration of a Perm-It™ infiltrometer.
Source: (American Manufacturing Company, Inc., 2021).

Figure 19: Conducting infiltrometer tests in the field using the Perm-It™ constant-head infiltrometer.

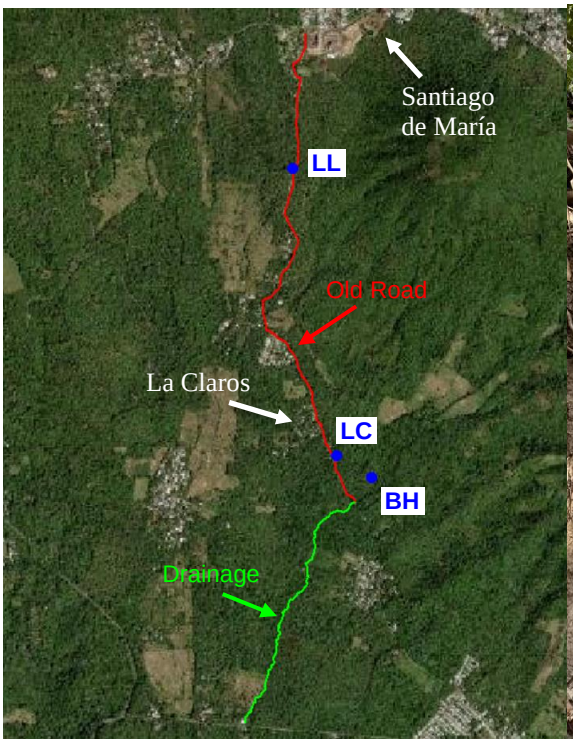

Figure 20: Infiltrometer test sites (blue dots).

Figure 21: Infiltrometer test soil cross-section.

2.2.3b Infiltrometer Tests Methods

The infiltration capacities and saturated hydraulic conductivities of surficial soils above the water table can be measured using infiltrometers. Infiltrometer tests are completed by creating temporary saturated soil conditions to determine K_{sat} and infiltration capacity simultaneously (American Manufacturing Company, Inc., 2021). To reach the constant head condition, a fixed suction pressure inside the upper cylinder of the device must be maintained. As the soil becomes saturated, a "bulb" of saturated soil conditions around the borehole will form (Figure 18). The constant-head infiltrometers utilize a Mariotte device configuration to supply water at a constant pressure from a reservoir (Figure 18). The flow is monitored until a constant (steady state) flow condition is reached.

The primary steps for conducting infiltrometer tests to determine K_{sat} (American Manufacturing Company, Inc., 2021) using the Permi-It™ infiltrometer include:

(1) Bore a clean, uniform hole at least 12 inches deep (record borehole depth in cm)
(2) Record the diameter of the borehole (D) in cm (r = D/2)
(3) Saturate the borehole and the subsurface around the borehole
(4) Fill the Permi-It™ infiltrometer upper cylinder
(5) Fill the borehole with water, quickly invert the infiltrometer, insert into the borehole, and start a timer
(6) Record the elapsed time every 100 cm^3 on the upper cylinder scale
(7) Once steady state has been reached, measure the stable height of water in the borehole from the top of the borehole
(8) Subtract the stable height of water in the borehole from the depth of borehole measured in step (1) to determine the height of water in borehole (H)
(9) The steady-state rate of water flow (Q) is determined by dividing water volume (cm^3) by Delta t (min)

2.2.3c Infiltrometer Tests Data

The infiltrometer test site name, average flow at steady state (Q), and average saturated hydraulic conductivity (K_{sat}) for sites BH, LC, and LL are displayed in Table 3. See Appendix D, Appendix E, and Appendix F for detailed tables containing infiltrometer test data for sites BH, LC, and LL. WEAP requires the saturated hydraulic conductivity to be in mm/timestep. In this study, each timestep consists of 15 minutes. After averaging the saturated hydraulic conductivity for BH, LC, and LL, the value is converted from cm/min to mm/15min (Table 4). The infiltrometer tests show that the average saturated hydraulic conductivity is 0.0213 cm/min (3.2 mm/15 min timestep).

Table 3: Average flow (Q) and average saturated hydraulic conductivity (K_{sat}).

Site	Average Flow at SS, Q (ml/min)	Average Saturated Hydraulic Conductivity, K_{sat} (cm/min)
BH	116.211	0.027
LC	59.422	0.014
LL	95.309	0.023

Table 4: BH, LC, and LL Average K_{sat}.

Total Average Saturated Hydraulic Conductivity, K_{sat} (cm/min)	0.0213
Total Average Saturated Hydraulic Conductivity, K_{sat} (mm/15 min)	3.2

2.2.4 Delineating Watersheds in ArcGIS Pro

WEAP does not enable users to import other DEM layers and the 90-meter resolution global DEM that WEAP uses does not provide the necessary resolution at the local scale for watershed delineation around California. Additionally, the DEM is unable to identify the La Claros drainage. Due to spatial limitations of the low-resolution WEAP DEM, ArcGIS Pro is used to delineate watersheds at the local scale. First, the Arc Hydro Tools Pro Toolbox is downloaded and installed (Esri, 2023). Within the Arc Hydro Toolbox under Terrain Preprocessing Workflows and then Dendritic, there is the Basic Dendritic Terrain Processing - No Fdr & Fac (Figure 22). This model can be used since Fill, Flow Direction, and Flow Accumulation tools were all run using the 10-meter DEM during previous watershed delineation.

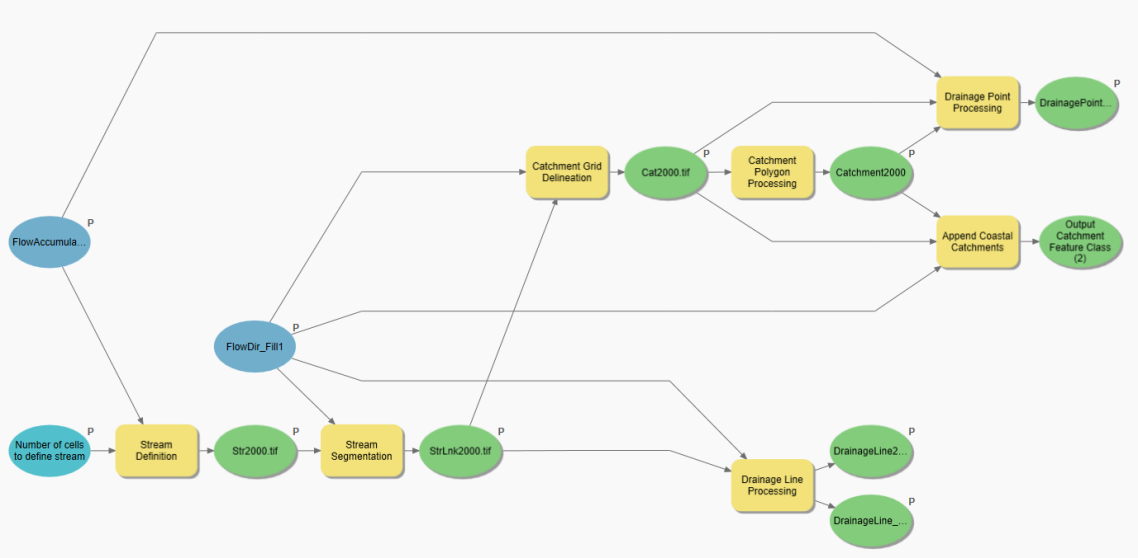

Figure 22: Basic Dendritic Terrain Processing - No Fdr & Fac Workflow. Source: (Esri, 2023).

The Input Flow Direction Raster and Input Flow Accumulation Raster are set to the corresponding layers created from the DEM. The number of cells to define stream is the stream definition threshold and is a function of contributing area. This sets the value for the flow accumulation raster (drainage density parameter) and changes how dense the river network is in the result. For example, setting the number of cells to define stream as a smaller number such as 100, would lead to a more significant number of rivers. This means that the workflow would result in a river under every 100 pixels of contributing area. Since the DEM in this study is a 10-meter DEM, each cell is 100 meters. 100 pixels multiplied by 100 meters is 10,000 square meters or .01 square kilometers. In the first trial, 500 was chosen as a starting value for number of cells to define stream. After running the workflow, it is determined that the number and size of reaches and catchments are too extensive for the purposes of flood modeling in WEAP. As a result, the workflow is run again with the value of 2000 for number of cells to define stream leading to fewer streams and catchments. The resulting catchments and drainage lines are shown in Figure 23.

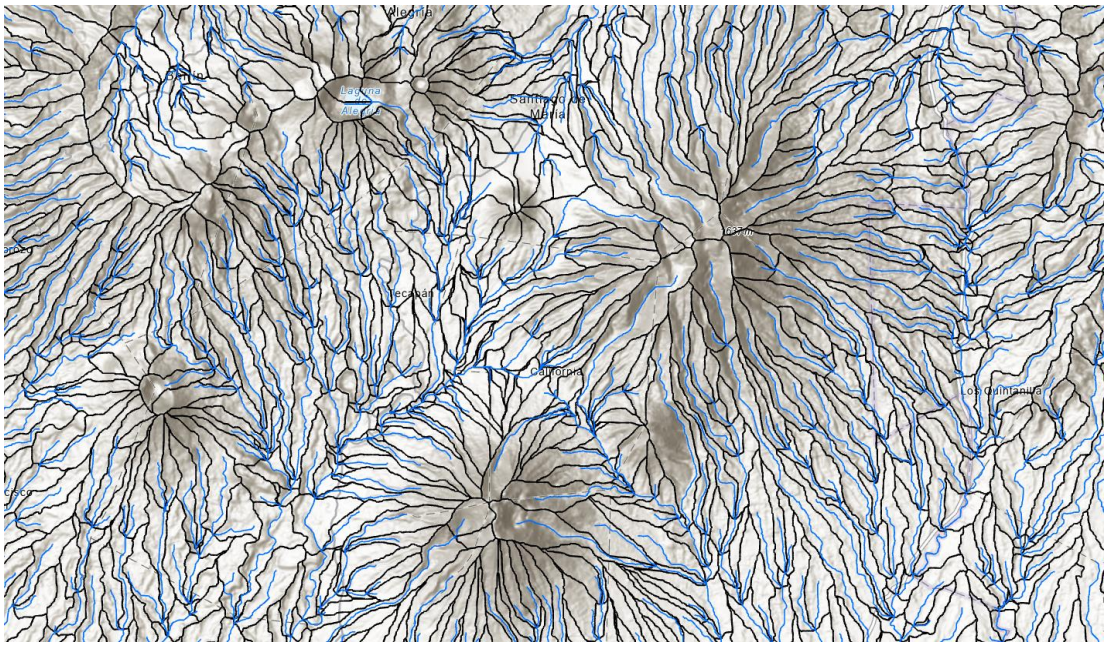

Figure 23: Resulting streams and catchments using the Basic Dendritic Terrain Processing - No Fdr & Fac Workflow. Source: (Esri, 2023).

2.2.5 Identifying Catchments in ArcGIS Pro

The drive from the La Claros drainage to Santiago de María and La Claros drainage path are used as a guide for determining the main drainage of focus based on the resulting drainage lines from the Basic Dendritic Terrain Processing Workflow (Figure 22). Using ArcGIS Pro, the tributaries connecting to the main drainage are used to identify 18 major catchments and associated catchment areas (total area of 25 km^2) (Figure 24). General tributary lengths are determined using the measure distance tool in ArcGIS Pro. See Appendix C Table C.1 for tributary lengths and contributing catchment areas for each tributary. The ArcGIS layer with the 18 catchments (T1-T18) are added to WEAP and these catchment boundaries are used to delineate one river for each catchment resulting in a 1:1 ratio for river:catchment (Figure 24).

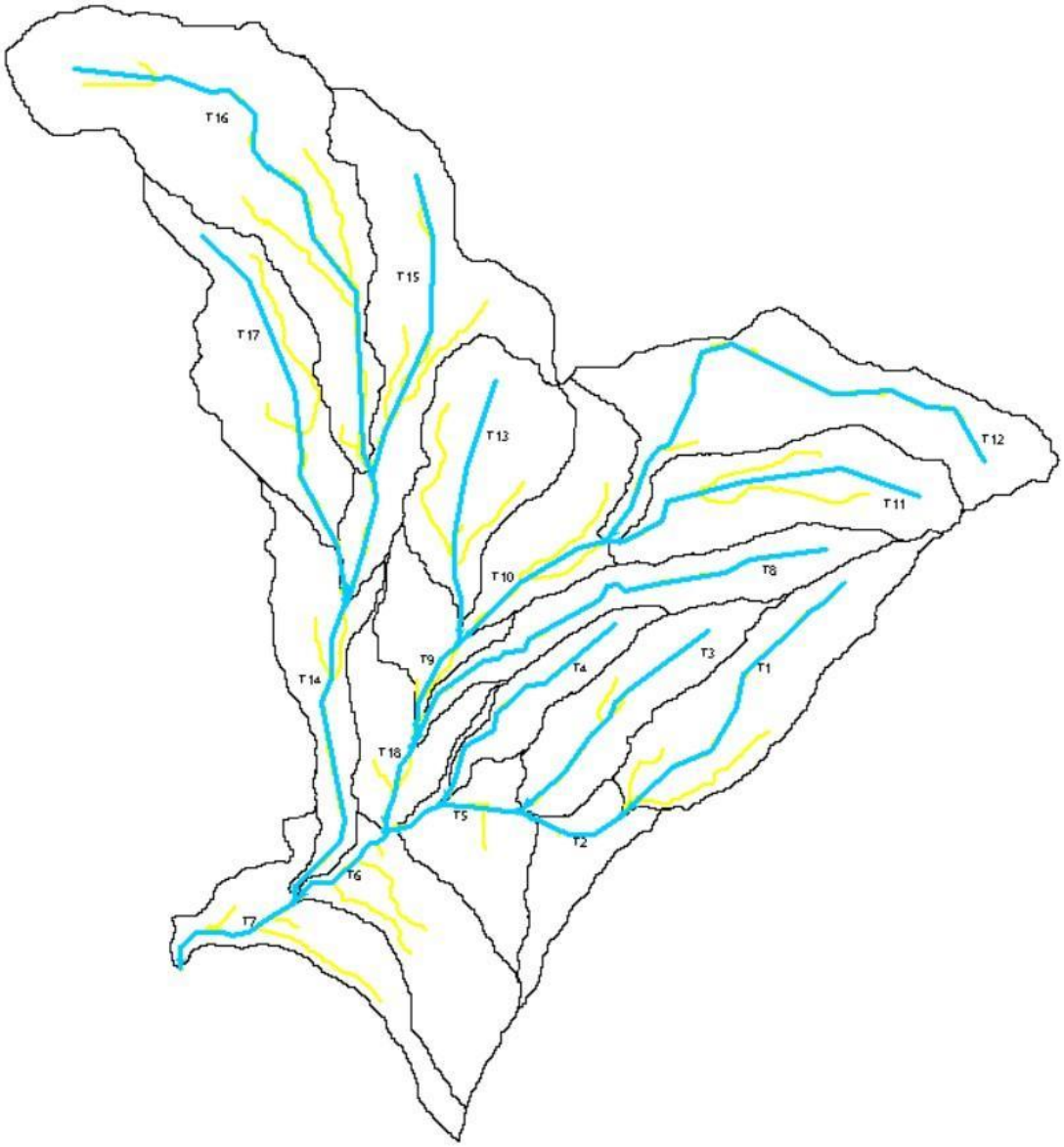

Figure 24: Delineating one river per catchment in WEAP.

2.2.6 Importing Data in WEAP

Catchments must be connected to the river element by using runoff/infiltration links from the catchment to the river. WEAP estimates the water balance of the catchment and transfers the outflow to the river through this link (Stockholm Environment Institute, 2023). A catchment node (green circle) and runoff/infiltration link (light blue dashed line) are added to each of the 18 catchments (Figure 25). The catchment area for each tributary and the tributary length of each catchment (Appendix C Table C.1) are added to WEAP by going to the data view and clicking on different features of the table of contents. By following the major branch, minor branch, and WEAP input within the table of contents under data view, each factor's value is added to all 18 catchments.

Local knowledge confirmed that when heavy precipitation occurs, Old Road (Figure 15) floods and flows into a drainage (Figure 16). Since the rivers that WEAP created do not reflect this significant human alteration (the road), a diversion feature is added to the model to reflect the flow from Old Road into the La Claros drainage. Diversion nodes withdraw water from a river and divert the flow down a different path. WEAP diverts the necessary amount of water needed to satisfy the connected demand sites and instream flow requirements unless fraction diverted is set (Stockholm Environment Institute, 1988).

The added diversion redirecting flow from the Old Road is displayed in Figure 25 and named RoadConveyance. The fraction diverted is estimated to be 80% assuming some flow is lost due to factors including infiltration. The conveyance can happen within the 15-min timestep, but we do not know the nature of the lag and do not have data to determine it. As a result, the travel time for the RoadConveyance is set to zero because it is assumed it only takes a few minutes for water at the top of the road to travel the road where it intercepts the La Claros drainage, which then captures that flood flow. The catchment where the diversion begins is split into two separate catchment areas. The contributing area (1.8 km^2) to the northern part of the catchment (CT15) is outlined in red in Figure 25. CT15 is the catchment contributing to the diversion (RoadConveyance). A catchment node and runoff/infiltration link are added to the southern part of the catchment (area 0.47 km^2) and labeled CT15_2.

Figure 26 displays three major nodes of interest in WEAP, which include where Old Road meets the La Claros drainage (RoadDrainage), the drainage ends and meets the flooded road (BananaCulvert), and where the tributaries all meet (T7_Tributary). WEAP inputs and equations can be represented by a two-bucket model (Figure 27). Table 5 displays each WEAP input location, name, description, value, and additional notes.

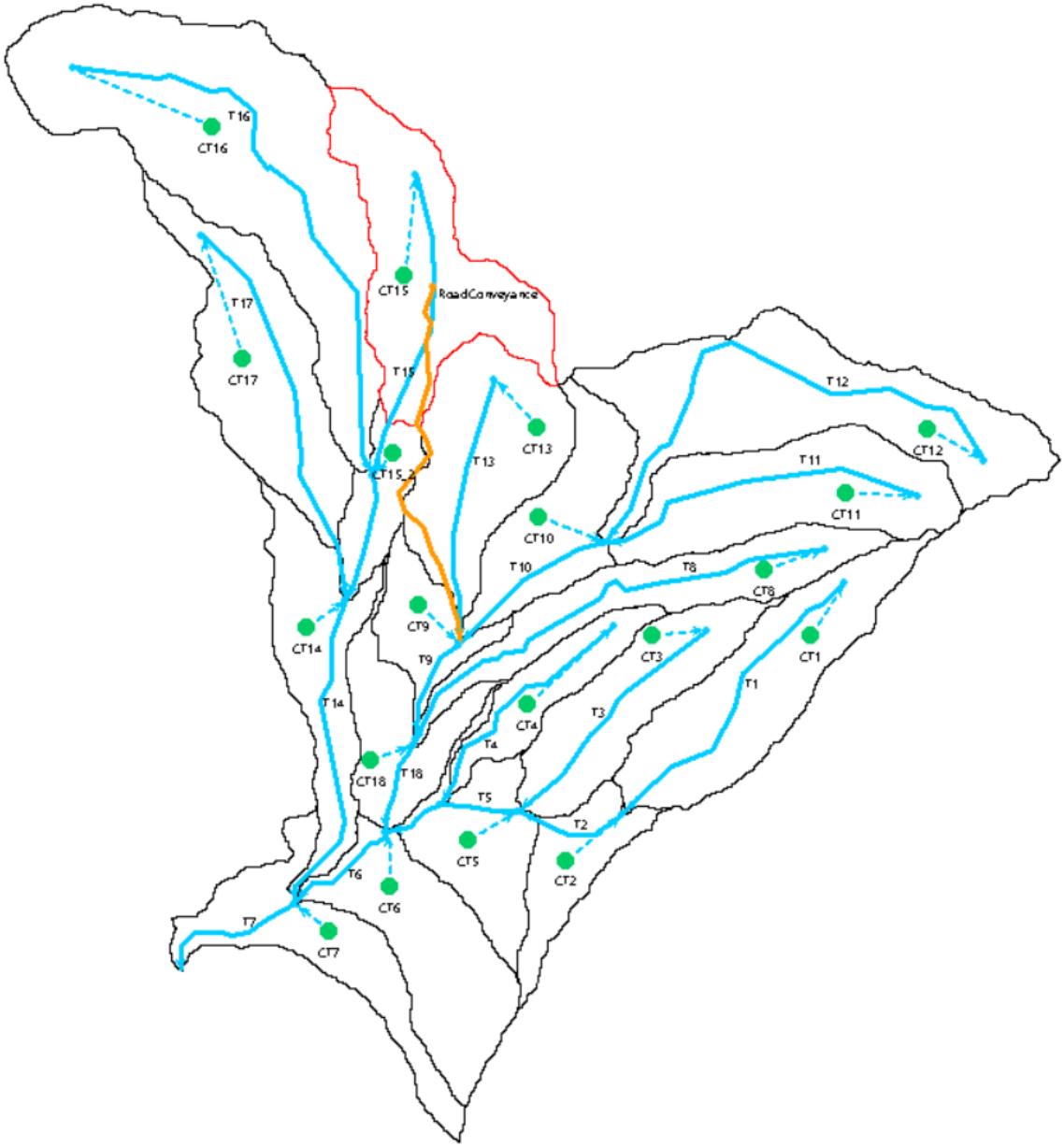

Figure 25: Catchment nodes and runoff/infiltration links in WEAP.

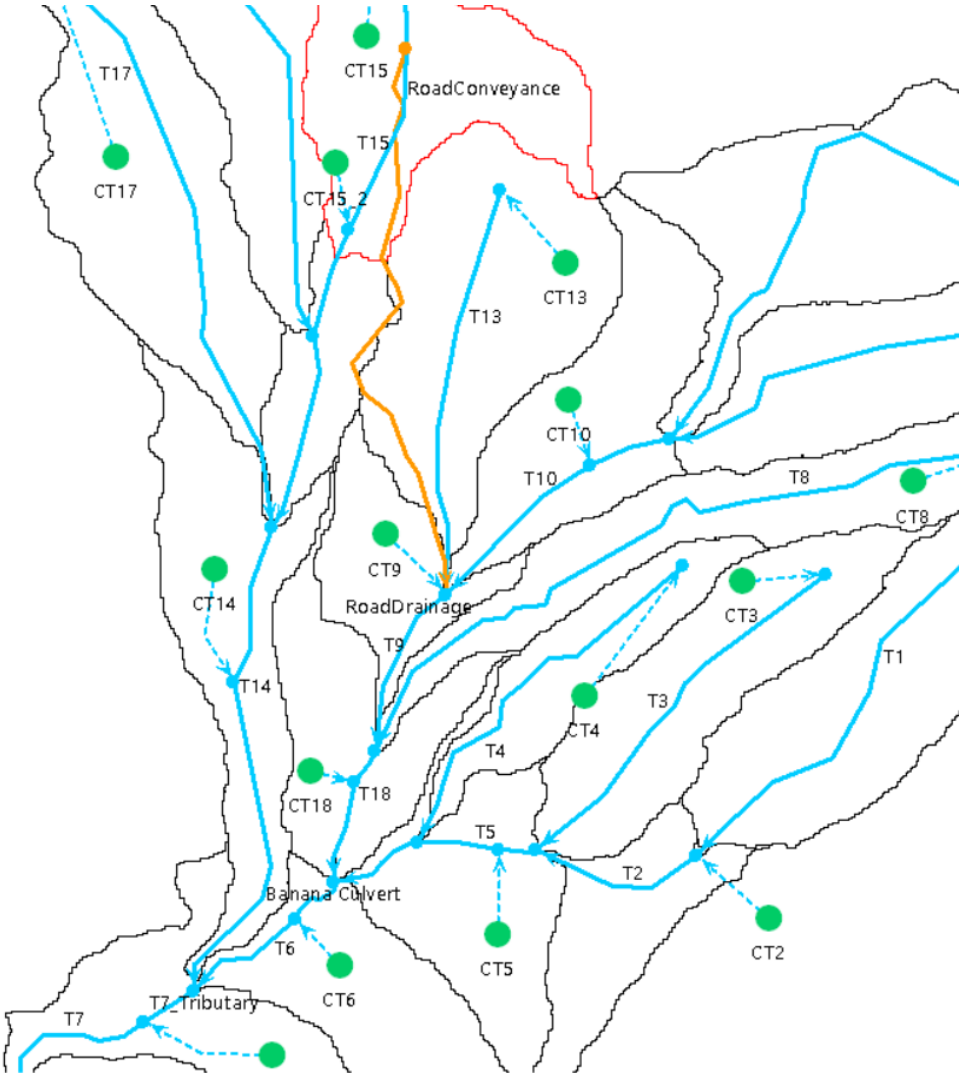

Figure 26: WEAP map showing major nodes of interest (RoadDrainage, BananaCulvert, and T7_Tributary).

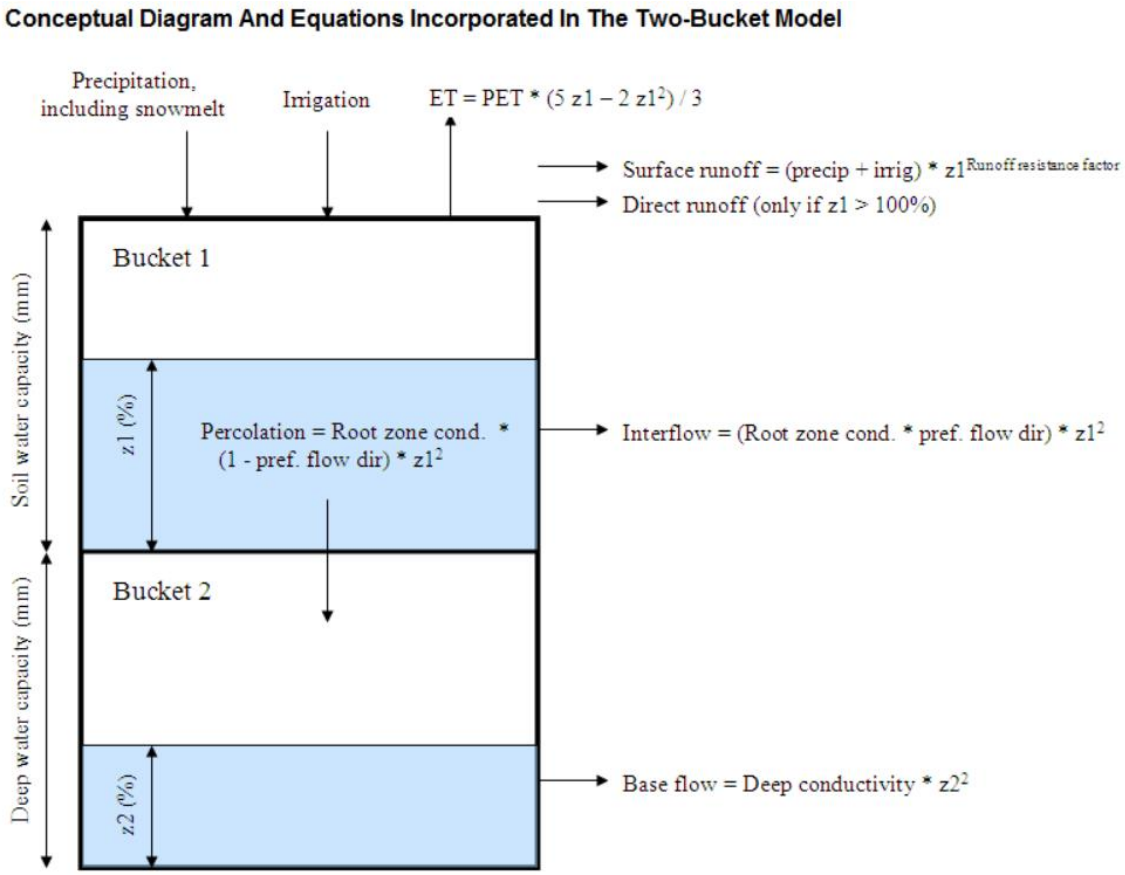

Figure 27: Conceptual diagram of WEAP inputs and equations.

Table 5: WEAP major and minor branches in the data view table of contents; WEAP input, description, and value; and additional notes. Source: (Stockholm Environment Institute, 1988).

Major Branch; Minor Branch	WEAP Input	WEAP Input Description	Value	Notes
Demand Sites and Catchments; Land Use	Area (km^2)	Land area for land cover class within branch or basin catchment.	Varies per catchment (Appendix C)	ArcGIS Pro Catchment Shape_Area
Demand Sites and Catchments; Land Use	Soil Water capacity (mm)	Effective water holding capacity of upper soil layer (top "bucket").	350	Average depth to borehole from infiltrometer tests
Demand Sites and Catchments; Land Use	Deep Conductivity (mm/timestep)	Conductivity rate (length/time) of the deep layer (bottom "bucket") at full saturation, which controls transmission of baseflow.	5	Baseflow will increase as deep conductivity increases
Demand Sites and Catchments; Land Use	Preferred Flow Direction	Used to partition the flow out of the root zone layer (top "bucket") between interflow and flow to the lower soil layer (bottom "bucket") or groundwater. 1.0=100% horizontal flow 0=100% vertical flow.	Varies per tributary (Appendix C)	Estimated tributary slope using DEM in ArcGIS Pro
Demand Sites and Catchments; Land Use	Initial Z1 (%)	Z1 is the relative storage given as a percentage of the total effective storage of the root zone water capacity.	5	Initial value for Z1 at the beginning of simulation
Demand Sites and Catchments; Land Use	Initial Z2 (%)	Z2 is the relative storage given as a percentage of the total effective storage of the lower soil bucket (deep water capacity).	10	Initial value for Z2 at the beginning of simulation
Demand Sites and Catchments; Land Use	Deep Water Capacity (mm)	Effective water holding capacity of lower, deep soil layer (bottom "bucket").	100	Given as a single value for the catchment and does not vary by land class type

Demand Sites and Catchments; Land Use	Runoff Resistance Factor	Controls surface runoff response. Related to factors such as leaf area index and land slope. Runoff tends to decrease with higher values.	Varies per catchment (Appendix C)	Estimated using WEAP background imagery; Scale 1(urban)-4 (forest)
Demand Sites and Catchments; Land Use	Root zone conductivity (mm/timestep)	Root zone (top "bucket") conductivity rate at full saturation, which will be partitioned, according to Preferred Flow Direction, between interflow and flow to the lower soil layer.	3.2	Average saturated hydraulic conductivity from infiltrometer tests
Demand Sites and Catchments; Climate	Precipitation (mm/timestep)	Precipitation time series can be read in from a file or entered manually. All branches within a catchment have the same climate data.	csv file	Vantage Pro2™ weather station rainfall data
Demand Sites and Catchments; Climate	ETref (mm)	Sub yearly evapotranspiration (ET) for a reference land class.	10/96	On average potential evaporative loss 10mm per day (96 timesteps)
Demand Sites and Catchments; Climate	Temperature (°C)	Weighted mean of high and low temperature on a monthly basis.	25°C	Vantage Pro2™ weather station averages 20-30°C
Demand Sites and Catchments; Climate	Latitude (decimal degrees)	Latitude in decimal degrees.	13	Latitude of California, El Salvador
Supply and Resources; Physical	Tailflow Point (km)	Distance of the reach.	Varies per tributary (Appendix C)	ArcGIS Pro Tributary Length
Supply and Resources; Physical	Travel Time	Number of timesteps for water to traverse the reach.	1	Below CT Runoff
Supply and Resources; Physical	Diffusion	In Muskingum equation, Storage=k(X Inflow + (1-X) Outflow), X is the diffusion parameter. Values must be between 0 and 0.5, with most rivers between 0.1 and 0.2.	0.15	Below T Headflow

2.3 WEAP Results

To determine the streamflow rate, the inflow and runoff are considered. In the streamflow rate output, the variable labeled inflow represents the points in the network where there is flow and connection of the network (light blue nodes). When selecting which river reaches and associated inflow to consider in the hydrograph, each catchment's inflow is displayed as "Below T# Inflow." This represents the flow downgradient (i.e., outflow) from that particular node. In that same variable (streamflow rate), runoff is the catchment's contribution to the network along the runoff/infiltration link (dashed blue line linking the catchment to the river). When selecting which river reaches and associated runoff to consider in the hydrograph, each catchment's runoff is displayed as "Below CT# Runoff".

The meteorological data collected by the Davis Vantage Pro2™ in California is displayed in Figure 28 from the start of data collection (August 11, 2021) through February 14, 2023, spanning a complete dry season (November 2021-April 2022) and a complete rainy season (May-October 2022). The time axis is based on the 15-minute timesteps, which is treated as a day in WEAP. The precipitation amount displayed on the vertical axis is the amount of precipitation recorded in 15-minute intervals. For the time period of 8/11/21-2/14/23, the peak precipitation was 28.4 mm on 5/3/22 (2166 in WEAP).

The precipitation in Figure 28 is the primary driver of the hydrology of the watersheds outlined in Figure 25. Some of the rainfall infiltrates the soil based on the measured hydraulic conductivities, as depicted in Figure 27, and some of the rainfall and soil moisture is calculated to evapotranspire back to the atmosphere based on solar intensity, air temperature, and relative humidity. WEAP then simulates hydrology for each timestep consecutively resulting in the overall hydrograph shown in Figure 29.

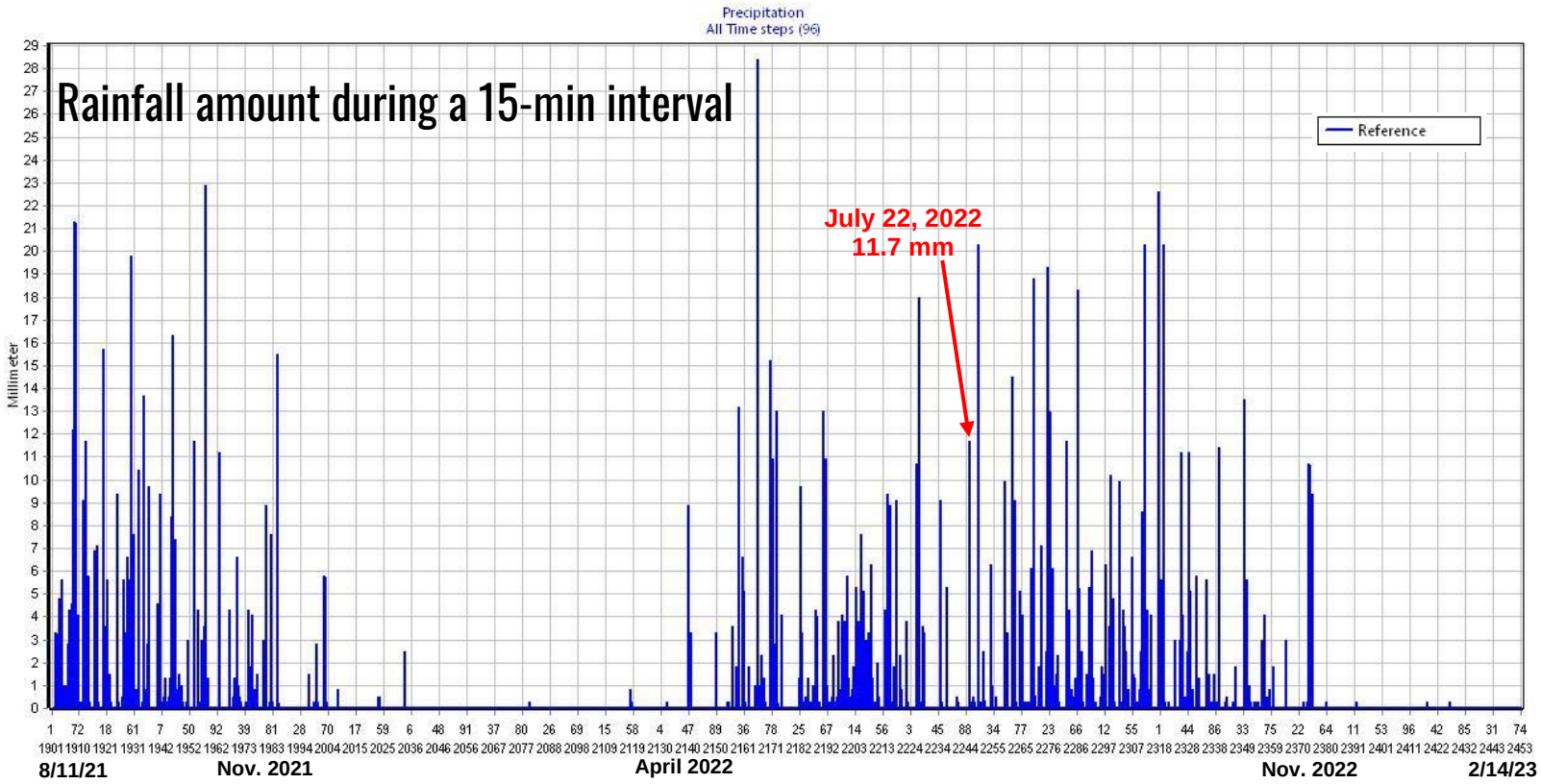

Figure 28: WEAP precipitation (mm) for all timesteps.

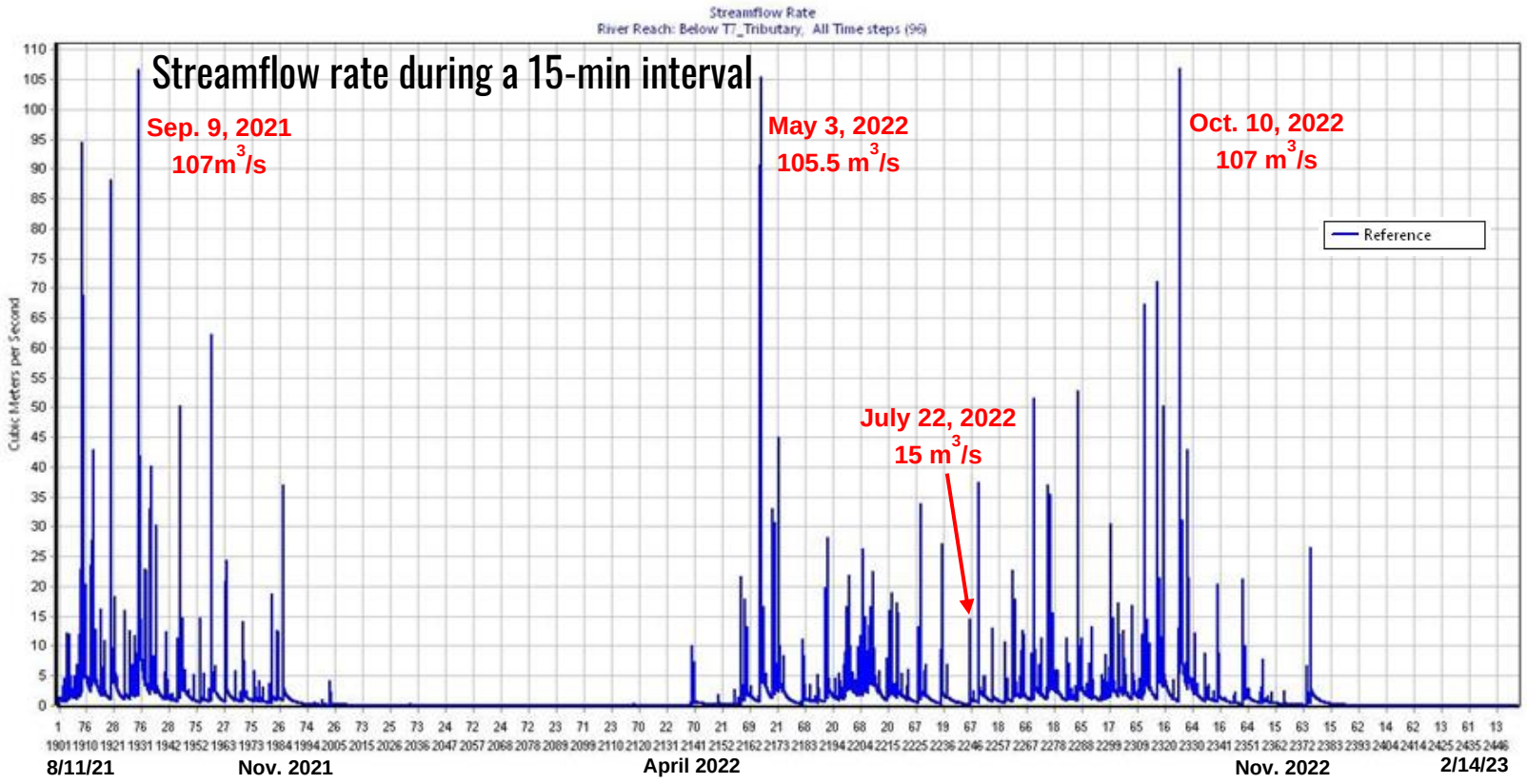

Figure 29: WEAP streamflow rate (m^3/s) below T7_Tributary for all timesteps.

Figure 29 shows the streamflow rate (m^3/s) below T7_Tributary (final tributary) for all timesteps. There is video evidence from a La Claros community local of a flash flood that occurred on July 22, 2022 (Figure 10). This date is used as a basis for investigating a specific flash flood event in more detail in WEAP. For 7/22/22 (2246 in WEAP), the precipitation graph (Figure 28) displays a value of 11.7mm and the streamflow rate graph (Figure 29) shows a value of 15 m^3/s.

The first streamflow rate peak occurred on 9/9/21 (1930 in WEAP) with a value of 107 m^3/s. The second major streamflow rate occurred on the date of the precipitation peak (5/3/22) with a streamflow rate of 105.5 m^3/s. The final streamflow rate peak occurred on 10/10/22 (2326) with a rate of 107 m^3/s.

Ideally, if flood events were recorded locally by community members in La Claros, they could be compared to the peak flows depicted in Figure 29. Approximate bankfull-flow calculations (Appendix B Table B.1) suggest that flooding of the road-drainage juncture is predicted to occur for peak flows greater than 3.60 m^3/s. Based on streamflow rates from Figure 29, any streamflow rate value exceeding 3.60 m^3/s would be classified as a flash flood, leading to an extreme number of flash floods. As a result, it is concluded that Manning's calculation is likely an overestimate of flash flooding. Using the 7/22/22 event streamflow rate value is seemingly a better basis from which to assume a potential flash flood threshold.

The peak height represents the maximum streamflow rate while the area under the curve is the cumulative volume of the flow. The WEAP streamflow rate (m^3/s) for below RoadDrainage, BananaCulvert, and T7_Tributary on 7/22/22 (2246 in WEAP) are compared in Figure 30. The peak streamflow rate for the RoadDrainage is 8 m^3/s, BananaCulvert is 10.25 m^3/s, and T7_Tributary is 15.25 m^3/s.

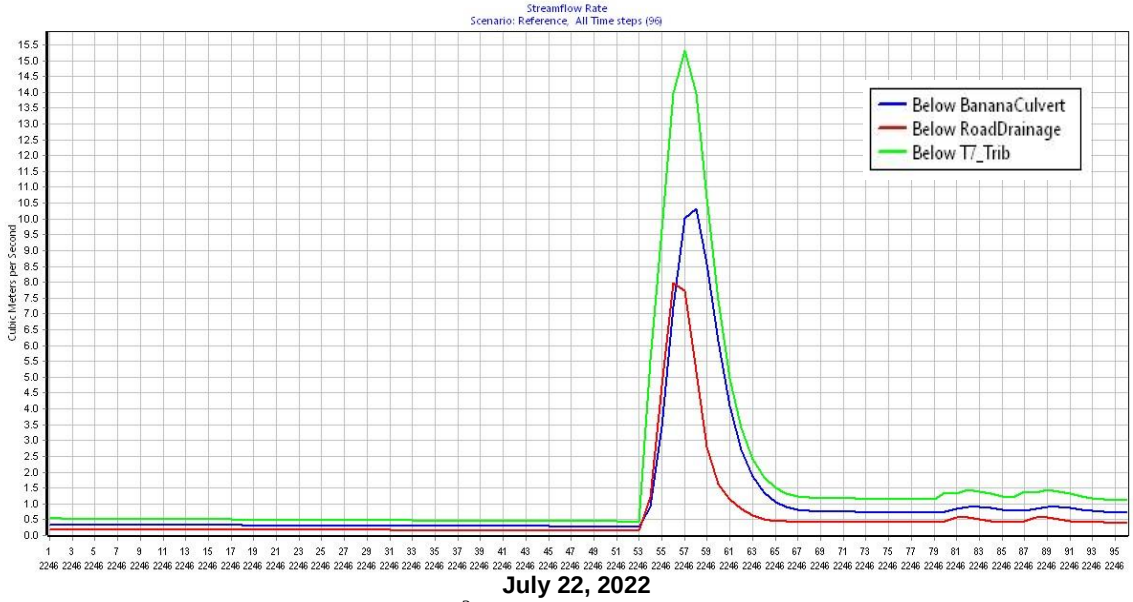

Figure 30: WEAP streamflow rate (m^3/s) comparison for RoadDrainage, BananaCulvert, and T&_Tributary on 7/22/22 (2246).

For the same date (7/22/22), the evapotranspiration (ET) is varied from 10/96 (mm/timestep) to 3.3/96 (mm/timestep) to test the streamflow rate's model sensitivity to ET. The ET is changed to 3.3mm based on ET estimates from the Vantage Pro2™ weather station and Penman-Monteith ET equation. Varying the ET in WEAP showed that the flash flood model is relatively insensitive to ET. Using the 7/22/22 date, the root zone conductivity (RZC) is varied from 3.2 (mm/timestep) to 5 (mm/timestep) to test the streamflow rate's model sensitivity to RZC. This results in the same peak streamflow rate of 10.25 m^3/s for both RZC values. After the streamflow rate begins to level out (around timestep 63 of WEAP year 2246), the streamflow rate with RZC of 5 mm/timestep is about 0.25 m^3/s greater than the streamflow rate with RZC of 3.2 mm/timestep (Figure 31). This small variance shows that the streamflow rate is relatively sensitive to RZC.

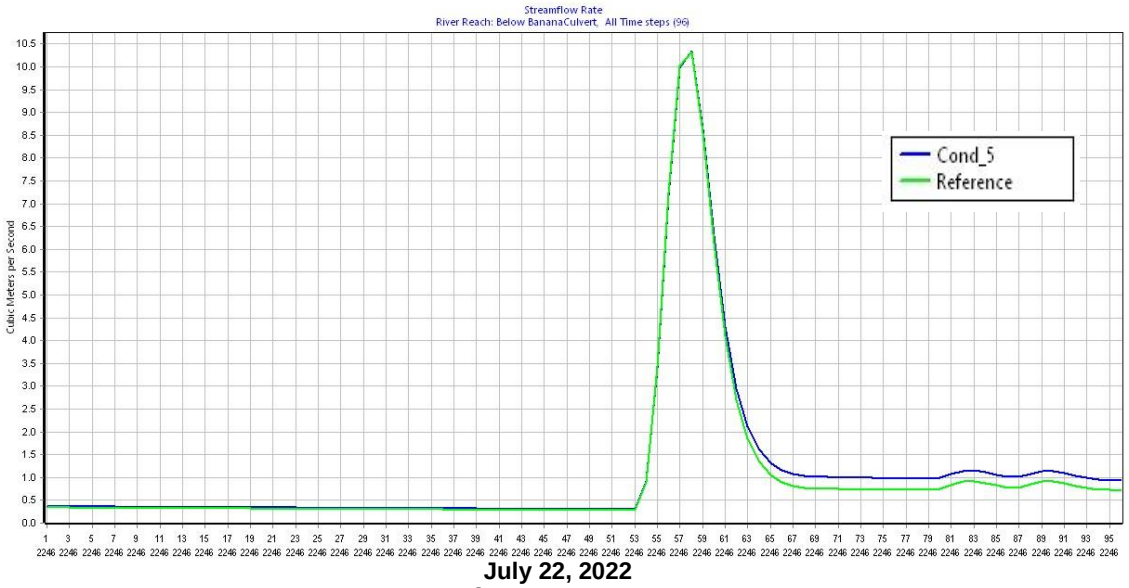

Figure 31: WEAP streamflow rate (m^3/s) root zone conductivity (RZC) comparison below BananaCulvert on 7/22/22 (2246). RZC of 5 (blue) and RZC of 3.2 (green).

In Figure 32, the streamflow rate below RoadDrainage (where Old Road meets the drainage) is compared for having the water go down RoadConveryance (Reference) in contrast to allowing the water flow down the natural drainage (CT15 to CT14). The peak streamflow rate with the road diversion is 8 m^3/s and peak streamflow rate without the road diversion is 4.75 m^3/s.

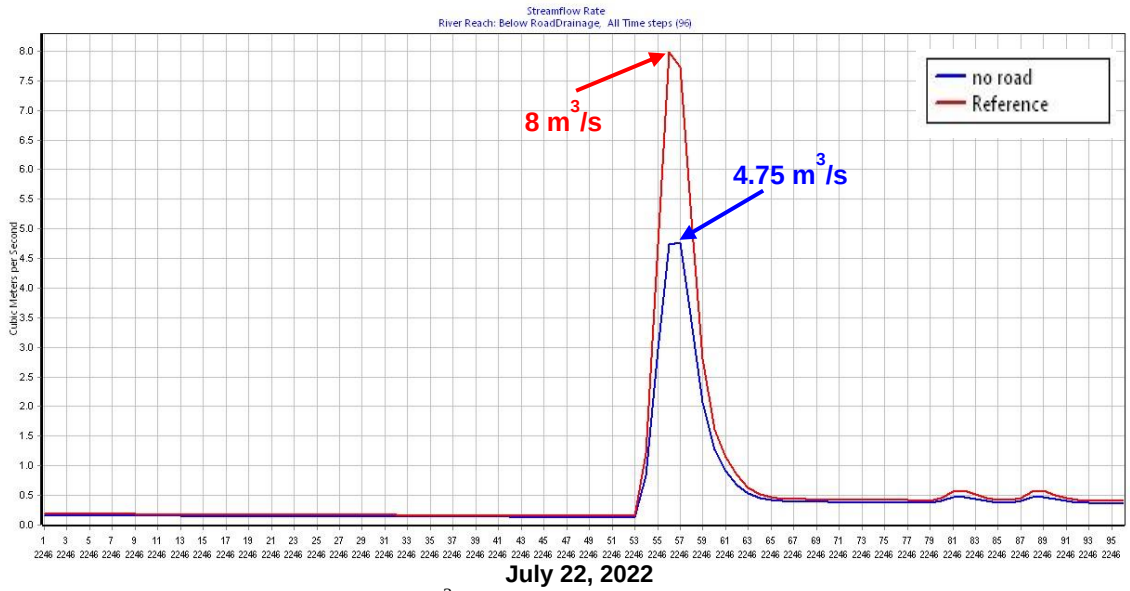

Figure 32: WEAP streamflow rate (m^3/s) road conveyance comparison below RoadDrainage on 7/22/22 (2246) using Davis data from California.

Old Road floods when the runoff from rainfall in Santiago de María that is diverted to and flows down Old Road exceeds the capacity of the ditches and drainages to convey the flows. The Ministry of Natural Resources and the Environment (MARN) records daily precipitation data from Santiago de María -- an urban (i.e., impermeable) environment upslope from Old Road. The daily precipitation data cannot accurately represent flash flood events at the sub-daily level like the Davis data from California which is in 15-minute intervals. This means the MARN rainfall data is likely a more realistic representation of the total amount of precipitation entering Old Road from Santiago de María compared to the Davis weather station data in California.

Using the July 22, 2022 event, the daily precipitation recorded by the MARN station was 72.7 mm versus the 23.3 mm recorded by the Davis station. The 15-minute intervals when it was raining the hardest in California were adjusted to reflect the total rainfall amount during the storm recorded in Santiago de María (72.2 mm). After modifying the 15-minute intervals for the Davis data, the WEAP model is run again for July 22, 2022 with CT15 (Santiago de María catchment - Figure 26) reflecting the increased precipitation values (Figure 33). The adjusted max streamflow rate of RoadDrainage with the RoadConveyance (Figure 33) is 14 m^3/s compared to the 8 m^3/s using the Davis data from California (Figure 32).

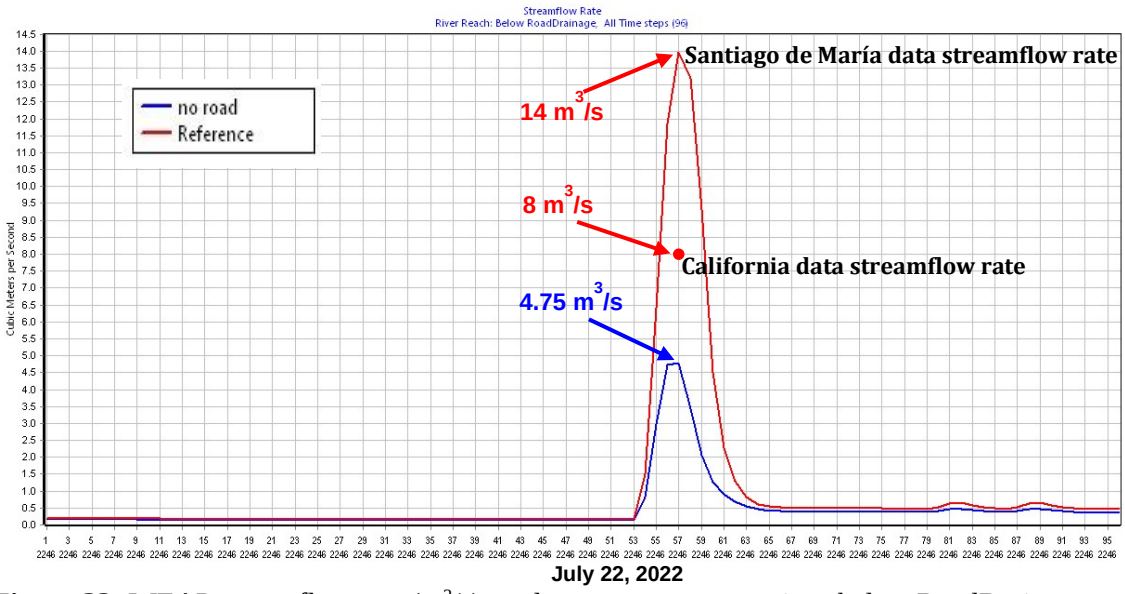

Figure 33: WEAP streamflow rate (m^3/s) road conveyance comparison below RoadDrainage on 7/22/22 (2246) using MARN data from Santiago de María.

2.4 WEAP Discussion

2.4.1 Flooding of Old Road

Since we have only one observational data set, we used Manning's equation (Appendix B Table B.1) to estimate when WEAP-estimated peak flows exceeded the primary constriction that causes flooding in La Claros (the culvert leads to flooding across that road). Once the flows reach the La Claros drainage, the middle part of the drainage likely conveys the highest flows, while the upper part of the drainage and the lower constrict for increased flooding. Additionally, the drainage would probably convey the rain events if the runoff from Santiago de María was not dumped on to Old Road.

The WEAP model results in a peak streamflow rate for the RoadDrainage of 8 m^3/s. This represents the location where the Old Road meets the La Claros drainage and where the drainage is narrower (2-m wide and 1-meter deep). Since Manning's equation estimates the bankfull flow to be 3.60 m^3/s, and the WEAP model estimates a peak streamflow rate of 8 m^3/s, this suggests the narrow section of the drainage would flood first. Where the channel is wider and deeper (6-m wide and 3-meter deep), it is more difficult to model the hydraulics as the water spreads across the landscape.

This study relies on rainfall data from the Vantage Pro2™ weather station in California. Rainfall data from this single weather station is used to reflect the precipitation in all 18 WEAP catchments leading to a data limitation where the weather station may not accurately reflect rainfall in certain catchments. Additionally, there are times when the weather station is missing data, likely due to power outages and internet connectivity issues leading to the inability to record data. For example, the flash flood event from 10/9/22-10/10/22 reflects one of the highest streamflow rate events in WEAP with a peak streamflow rate of 107 m^3/s. This event is missing 35 timesteps (35 15-minute intervals) of rainfall data from an internet outage – likely because the power was knocked out during this storm. This means the rainfall data could lead to the potential underestimation of flash flood streamflow rates.

The Davis rainfall data in California is adjusted for catchment 15 to represent the amount of precipitation that occurred on July 22, 2022 in Santiago de María. Rainfall in areas of western Santiago de María runs off to drains that convey down Old Road during heavy rainfall events. Adjusting the Davis data led to a 1.75X increase for the July 22, 2022 event from 8 m^3/s (Figure 32) to 14 m^3/s (Figure 33). WEAP still registered the flood event on July 22, 2022 using the original Davis data, however the magnitude of the event is underestimated compared to using the MARN data. This represents the need for increased monitoring of precipitation data from more locations to provide a more comprehensive result in WEAP compared to relying on one station from one point that is located at one of the lowest elevations throughout the watersheds. The assumption that the MARN daily rainfall data can reflect the rainfall being diverted down Old Road is limited by the low temporal resolution (daily) of the MARN data.

2.4.2 WEAP Hydrographs

The eight highest streamflow rates (8/11/2 - 2/14/23) are determined from WEAP (Figure 29). Each date where a peak streamflow rate occurs is correlated with the Vantage Pro2™ weather station rainfall data to determine antecedent rainfall conditions and total precipitation (excluding antecedent precipitation) for each flash flood event (Table 6). For flash flooding based on the Davis rainfall data, antecedent precipitation does not have a large impact on whether a flash flood event occurs, or not as multiple flash flood events have 0 mm of antecedent precipitation (Table 6). Despite having no antecedent precipitation for some events, a flash flood can still occur due to the high rainfall intensity of the event. Precipitation at the flash flood location is not the only factor from which to base flash flooding potential. Locals expressed that there are times when it is raining in Santiago de María and not raining in California, but the water from Santiago de María floods California.

Table 6: WEAP peak streamflow rates and associated antecedent and total precipitation.

Date	WEAP Date	Peak Streamflow Rate (m^3/s)	Antecedent Precipitation (mm)	Total Precipitation (mm)
8/19/21	1909	95	19.8	52.5
8/30/21	1920	88	0	64.9
9/9/21-9/10/21	1930-1931	107	0	70
10/6/21-10/7/21	1957-1958	62.5	4.7	39.7
5/3/22-5/4/22	2166-2167	105.5	4.9	67.5
9/25/22-9/26/22	2311-2312	67.5	17.1	40.1
10/1/22	2317	71	0	51
10/9/22-10/10/22	2325-2326	107	54.6	61.7

Antecedent rainfall conditions have a large influence on the final flood magnitude, so as a result streamflow rate is run for 7/20/22 (2244 in WEAP) - 7/22/22 (2246 in WEAP). There is no precipitation that occurs before the 7/22/22 flood event leading to antecedent conditions with a lower soil moisture content.

Old Road (Figure 15) is represented by a diversion called RoadConveyance in WEAP. This road leads from Santiago de María, past La Claros, and into the La Claros drainage (Figure 16). This drainage ends at a banana culvert and main road which floods

during heavy precipitation events. In Santiago de María, a storm sewer was built to divert water into the ditches along the side of Old Road. This work attempted to determine whether flooding would still occur in La Claros if rainwater from Santiago de María was diverted down its natural drainage instead of artificially down Old Road.

The estimate from Manning's equation suggests that if the flow is greater than 3.60 m^3/s, it will flow out of the bank. The WEAP model results in a graph for 7/22/22 (Figure 32) where peak streamflow rate with the road diversion is 8 m^3/s and peak streamflow rate without the road diversion is 4.75 m^3/s. The flow from the road diversion is an approximation, and based on Manning's estimate, both streamflow rates would flow out of the bank. In general, the peak streamflow rate with the road diversion is much greater leading to higher risk of exceeding the bankfull flow.

These results do not necessarily mean that the La Claros community would not still experience flash flooding if water was not diverted from Santiago de María as there are many factors that contribute to flash flooding. However, the results do show that streamflow rate is higher with the road diversion from Santiago de María than if the flow were to follow the natural drainage. It is a possibility that dumping the storm water from Santiago de María on to Old Road may overwhelm the road's ditch capacity leading to flash flooding. Theoretically, WEAP could have been used when the road was built to determine how much water runoff was going to be channeled into La Claros and aid in decision making.

2.5 Limitations and Suggestions

The ArcGIS Pro flash flood susceptibility map and WEAP flash flood modeling were both limited by data availability. This includes the lack of a higher resolution DEM that would enable more detailed and accurate modeling at the local scale. The study was also limited by the single weather station with areas of missing rainfall data and three infiltrometer test sites being the only infiltration data. Both the rainfall data and infiltrometer data were used to characterize all 18 WEAP catchment areas and may not accurately reflect each catchment. In general, there is a lack of data availability regarding hydrologic factors related to flash flooding at the local scale in El Salvador. This is due to the need for better monitoring of precipitation and flash flooding events (time, duration, and intensity). There is also a lack of data for geologic characterization and land use at the local scale in El Salvador, both of which are important in flash flood modeling. The Ministry of Environment and Natural Resources has a website that displays river gauges in El Salvador (Ministerio de Medio Ambiente y Recursos Naturales), however there is no monitoring being conducted proximal to California. In addition, there are limited river gauges with flow history and the gauges that do have flow history only display monthly data (needed sub-daily for flash flood modeling). The Ministry of Environment has a record of weather-related events that triggered them to issue a "Special Bulletin" (Ministerio de Medio Ambiente) which includes hurricanes, tropical storms, tropical depressions, tropical waves, etc. While these events are important, they are national events which do not always reflect events at the local scale, especially short duration

events like flash flooding. Model results will be improved with longer data sets; however, I was limited to the data available during my two year masters program.

I suggest creating a network of community members who are local observers of flash flood events. This network would keep a systematic record of events to provide evidence that could be correlated with my model and used for future research to better understand flood hazards in the area. It would also be helpful to measure the river stage and train locals to use the equipment and report the data to groups such as Civil Protection.

2.6 Contribution to Literature

Despite the study area receiving ~2 m of rain/per year, there is no surface water and a lack of reliable access to potable water. My study can provide insight into how a region with intense precipitation has no surface water, an initial step in understanding groundwater hydrology in the area. One of the project's partners, Lutheran World Relief, also works to reduce risk to natural hazards and address water scarcity in the study area. They have identified the California community as a target for disaster risk reduction intervention and their most recent project, Phase II SOS, specifically has a hydrologic focus. As a result, my research can contribute to their efforts to understand hydrologic hazards in the area, specifically flash floods. In addition to Lutheran World Relief, my project will expand the data available to other in-country partners including the Dirección General de Protección Civil (Civil Protection), whose focus is the prevention and mitigation of disasters. My ArcGIS Pro flash flood susceptibility map and WEAP model will provide a visual output that is useful for education/outreach, disaster risk reduction, and evacuation planning.

3 Conclusions

The goal of this study was to improve understanding of flash-flood hazards in remote, low-resource communities. A regional flash-flood susceptibility map of the Usulután Department, El Salvador was created using ArcGIS Pro. The map provides a qualitative topographic ranking of flash-flood susceptibility based on elevation, slope, Euclidean distance, LULC, and rainfall. This product was shown to local Civil Protection officials to integrate their knowledge of flooding events in the areas they are responsible for in the Department of Usulután. Their information was valuable in terms of the extents, locations, and timing of flooding events to help improve the “best fit” match for the weighted overlay approach to flash flood modeling. The Water Evaluation and Planning system (WEAP) was used to model sub-daily flash flooding events at the local scale in a data-poor region for the first time. The area of focus included watersheds within the municipal region of California, El Salvador. Field work, climate data, topography, soil infiltration rates, and other estimated variables are input into WEAP to

model flash-flood events by simulating time-varying streamflow rates for various scenarios. By comparing WEAP–model estimates of major flash-flood events to rainfall data, it was determined that a flash flood can still occur without antecedent precipitation. This is likely due to the high rainfall intensity of the event in addition to water being diverted from Santiago de María. The analysis of flash flooding at the local scale provided key information for better understanding flash flood risk in the municipal region of California. It is hoped that this study will promote further monitoring of rainfall and land use change, encourage increased incorporation of local knowledge to improve future flash flood research, and inspire future flash flood mapping and modeling in data-poor regions.

4 References

Abdelkareem, M., 2017. Targeting flash flood potential areas using remotely sensed data and GIS techniques. *Natural Hazards*, 85(1), pp.19-37.

Agarwal, S., Patil, J.P., Goyal, V.C. and Singh, A., 2019. Assessment of water supply–demand using water evaluation and planning (WEAP) model for Ur River watershed, Madhya Pradesh, India. Journal of The Institution of Engineers (India): Series A, 100, pp.21-32.

Allafta, H. and Opp, C., 2021. GIS-based multi-criteria analysis for flood prone areas mapping in the trans-boundary Shatt Al-Arab basin, Iraq-Iran. Geomatics, Natural Hazards and Risk, 12(1), pp.2087-2116.

American Manufacturing Company, Inc. (2021) *PERM-IT™ Permeameter*. Available at: https://www.americanonsite.com/wp-content/uploads/2021/05/PERMEAMETER-USERS-MANUAL.pdf (Accessed: 15 March 2023).

Amoozegar, A., 2002, January. Models for field determination of saturated hydraulic conductivity. In XLV Annual Meeting. Raleigh, NC, USA (pp. 45-53).

Bajabaa, S., Masoud, M., and Al-Amri, N., 2014. Flash flood hazard mapping based on quantitative hydrology, geomorphology and GIS techniques (case study of Wadi Al Lith, Saudi Arabia). Arabian Journal of Geosciences, 7(6), pp.2469-2481.

CHRS 2019, UCI CHRS Data Portal-PDIR-Now. ArcGrid, 28 October 2022, <https://chrsdata.eng.uci.edu/>.

Claure, P., Esquivel, N.N., Liera, C., Trujillo, A.S. and Escobar, M., 2023. Introducing the WASH Flows analytical tool.

Costache, R., Pham, Q.B., Sharifi, E., Linh, N.T.T., Abba, S.I., Vojtek, M., Vojteková, J., Nhi, P.T.T. and Khoi, D.N., 2019. Flash-flood susceptibility assessment using multi-criteria decision making and machine learning supported by remote sensing and GIS techniques. *Remote Sensing*, 12(1), p.106.

Create points from a table (2021) Available at: https://pro.arcgis.com/en/pro-app/latest/get-started/create-points-from-a-table.htm (Accessed: 7 February 2023).

Curebal, I., Efe, R., Ozdemir, H., Soykan, A. and Sönmez, S., 2016. GIS-based approach for flood analysis: Case study of Keçidere flash flood event (Turkey). *Geocarto International*, 31(4), pp.355-366.

Dawod, G.M., Mirza, M.N. and Al-Ghamdi, K.A., 2011. GIS-based spatial mapping of flash flood hazard in Makkah City, Saudi Arabia. Journal of Geographic Information System, 3(03), p.225.

Departments of El Salvador (2023) Available at: https://en.wikipedia.org/wiki/Departments_of_El_Salvador#References (Accessed: 10 February 2023).

Elkhrachy, I., 2015. Flash flood hazard mapping using satellite images and GIS tools: a case study of Najran City, Kingdom of Saudi Arabia (KSA). The Egyptian Journal of Remote Sensing and Space Science, 18(2), pp.261-278.

Esri (2015) *ArcGIS Pro* (Version 3.0.3) [Computer program]. Esri Inc.

Esri (2023) *Arc Hydro* (Version 3.0.44) [Computer program]. Esri Inc.

FAO, 2016. Dry Corridor Central America: Situation Report June 2016.

Fard, M.D. and Sarjoughian, H.S., 2020, May. Coupling WEAP and LEAP models using interaction modeling. In 2020 Spring Simulation Conference (SpringSim) (pp. 1-12). IEEE.

Foroodi Safat, E., Ahmadi, M.M., Qaderi, K. and Golestani Kermani, S., 2021. Evaluation of two combined hydrological-black box models for flood forecasting in Halilrud river basin. Iranian journal of Ecohydrology, 8(2), pp.397-409.

Gobierno de El Salvador. *Centro Nacional de Registros*. Available at: https://www.cnr.gob.sv/ (Accessed: 9 December 2022).

Google (2022) *Google Earth Pro* (Version 7.3.6.9345) [Computer program]. Google LLC.

Gotlieb, Y., Pérez-Briceño, P.M., Hidalgo, H.G. and Alfaro, E.J., 2019. The Central American Dry Corridor: a consensus statement and its background. *Yu'am" Revista Mesoamericana de Biodiversidad y Cambio Climático*, 3(5), pp.42-51.

Hadded, R., Nouiri, I., Alshihabi, O., Maßmann, J., Huber, M., Laghouane, A., Yahiaoui, H. and Tarhouni, J., 2013. A decision support system to manage the groundwater of the zeuss koutine aquifer using the WEAP-MODFLOW framework. Water resources management, 27, pp.1981-2000.

Hamed, A.A., Sayed, M.E. and Meshari, L., 2020. Assessment of future water, energy, and food nexus by using WEAP and LEAP model in the state of Kuwait. Journal of Environmental Science, 49(9), pp.495-526.

Hamlat, A., Errih, M. and Guidoum, A., 2013. Simulation of water resources management scenarios in western Algeria watersheds using WEAP model. Arabian Journal of Geosciences, 6, pp.2225-2236.

Hidalgo, H.G. and Alfaro, E.J., 2012. Some physical and socio-economic aspects of climate change in Central America. Progress in Physical Geography, 36(3), pp.379-399.

Höllermann, B., Giertz, S. and Diekkrüger, B., 2010. Benin 2025—Balancing future water availability and demand using the WEAP 'Water Evaluation and Planning' System. Water resources management, 24, pp.3591-3613.

Impact Observatory, Microsoft, and Esri 2022, Esri Land use/land cover in 2017, 2018, 2019, 2020, 2021, Global. GeoTIFF, viewed 28 October 2022, <https://www.arcgis.com/apps/mapviewer/index.html?layers=cfcb7609de5f478eb7666240902d4d3d>.

Kavand, H., Ziaee, S. and Mardani, M., 2020. Assessing the consequences of internalization of the side effects of water pollution on the quantitative and qualitative management of Zayandehroud Basin. Journal of Agricultural Economics and Development, 34(3), pp.341-356.

Lévite, H., Sally, H. and Cour, J., 2003. Testing water demand management scenarios in a water-stressed basin in South Africa: application of the WEAP model. Physics and Chemistry of the Earth, Parts A/B/C, 28(20-27), pp.779-786.

Liu, G., Hu, J., Chen, C., Xu, L., Wang, N., Meng, F., Giannetti, B.F., Agostinho, F., Almeida, C.M. and Casazza, M., 2021. LEAP-WEAP analysis of urban energy-water dynamic nexus in Beijing (China). Renewable and Sustainable Energy Reviews, 136, p.110369.

Li, X., Zhao, Y., Shi, C., Sha, J., Wang, Z.L. and Wang, Y., 2015. Application of Water Evaluation and Planning (WEAP) model for water resources management strategy estimation in coastal Binhai New Area, China. Ocean & Coastal Management, 106, pp.97-109.

Manning's n values (2006) Available at: https://www.fsl.orst.edu/geowater/FX3/help/8_Hydraulic_Reference/Mannings_n_Tables.htm (Accessed: 3 April 2023).

MapScaping Aps (2022) *Flood Risk Modelling*. Available at: https://mapscaping.com/flood-risk-modelling/ (Accessed: 9 December 2022).

Ministerio de Medio Ambiente. *Archivo de Informes Especiales.* Dirección General de Observatorio de Amenazas y Recursos Naturales. Available at: http://www.snet.gob.sv/ver/meteorologia/informes+especiales/archivo/ (Accessed: 12 April 2023).

Ministerio de Medio Ambiente y Recursos Naturales. *Aguas superficiales.* Sistema de Información Hidrológica. Available at: http://srt.snet.gob.sv/sihi/public/app/3/aforos (Accessed: 12 April 2023).

Moein, M.K., Shabanlou, S. and Fathian, H., 2013. Simulation of Flood Occurrence Using WEAP Model.

Mohamed, S.A. and El-Raey, M.E., 2020. Vulnerability assessment for flash floods using GIS spatial modeling and remotely sensed data in El-Arish City, North Sinai, Egypt. *Natural Hazards*, 102(2), pp.707-728.

Mounir, Z.M., Ma, C.M. and Amadou, I., 2011. Application of water evaluation and planning (WEAP): A model to assess future water demands in the Niger River (in Niger Republic). Modern Applied Science, 5(1), p.38.

Normal depth calculator. Available at: https://www.weather.gov/aprfc/NormalDepthCalc (Accessed: 3 April 2023).

onXmaps, Inc. (2023) *onXMaps.* Version 23.7.0. [Mobile app]. Apple App Store.

Oppong, J., (2021) *How to Use ArcGIS Pro to Map Flood Susceptibility*. Available at: https://www.gislounge.com/how-to-use-arcgis-pro-to-map-flood-susceptibility/#:~:text=First%2C%20open%20a%20new%20project,DEM%20onto%20the%20map%20canvas. (Accessed: 24 October 2022).

Oxford reference (2023) Available at: https://www.oxfordreference.com/display/10.1093/oi/authority.20110803095445221;jsessionid=E0FE0D1E521E847D6D157C22AD7D528F (Accessed: 3 April 2023).

Pérez-Briceño, P.M., Alfaro, E.J., Hidalgo, H. and Jiménez, F., 2016. Distribución espacial de impactos de eventos hidrometeorológicos en América Central. Revista de Climatología, 16, pp.63-75.

Pham, B.T., Avand, M., Janizadeh, S., Phong, T.V., Al-Ansari, N., Ho, L.S., Das, S., Le, H.V., Amini, A., Bozchaloei, S.K. and Jafari, F., 2020. GIS based hybrid computational approaches for flash flood susceptibility assessment. *Water*, 12(3), p.683.

Raskin, P., Hensen, E., Zhu, M., and Stavisky, D., 1992. Simulation of water supply and demand in the Aral Sea region. *Water International*, 17(2), pp.55-67.

Regional Initiative for the Dry Corridor (2022) Available at: https://www.fao.org/hand-in-hand/investment-forum-2022/the-dry-corridor/en (Accessed: 19 October 2022).

Schumacher, R.S., 2017. Heavy rainfall and flash flooding. In Oxford Research Encyclopedia of Natural Hazard Science.

Shakak, N.B.I., 2022. Simulation of Environmental Pollution Using Advance Technology and Modeling. The International Archives of Photogrammetry, Remote Sensing and Spatial Information Sciences, 43, pp.23-29.

Sieber, J. and Purkey, D., 2015. WEAP user guide. Somerville, MA (USA).

Stockholm Environment Institute (1988) *Water Evaluation And Planning* (Version 2022.0, October 25, 2022) [Computer program]. Available at: https://www.weap21.org/index.asp?action=40 (Downloaded: 7 February 2023).

Stockholm Environment Institute (2023) *Welcome to WEAP!* Available at: https://www.weap21.org/index.asp?action=200 (Accessed: 7 February 2023).

Swain, K.C., Singha, C. and Nayak, L., 2020. Flood susceptibility mapping through the GIS-AHP technique using the cloud. ISPRS International Journal of Geo-Information, 9(12), p.720.

Tutorial, S.W., 2016. Stockholm Environment Institute: Stockholm.

Usulután, El Salvador Genealogy (2022) Available at: https://www.familysearch.org/en/wiki/Usulut%C3%A1n,_El_Salvador_Genealogy (Accessed: 10 February 2023).

Van der Zee Arias, A., Van der Zee, J., Meyrat, A., Poveda, C. and Picado, L., 2012. Estudio de caracterización del Corredor Seco Centroamericano. *FAO Food and Agriculture Organization of the United Nations*, pp.1-91.

Vantage Pro2™ (2023) Available at: https://www.davisinstruments.com/pages/vantage-pro2 (Accessed: 15 February 2023).

Yariyan, P., Avand, M., Abbaspour, R.A., Torabi Haghighi, A., Costache, R., Ghorbanzadeh, O., Janizadeh, S. and Blaschke, T., 2020. Flood susceptibility mapping using an improved analytic network process with statistical models. Geomatics, Natural Hazards and Risk, 11(1), pp.2282-2314.

Youssef, A.M., Pradhan, B. and Hassan, A.M., 2011. Flash flood risk estimation along the St. Katherine road, southern Sinai, Egypt using GIS based morphometry and satellite imagery. *Environmental Earth Sciences*, 62(3), pp.611-623.

Zaharia, L., Costache, R., Prăvălie, R. and Minea, G., 2015. Assessment and mapping of flood potential in the Slănic catchment in Romania. Journal of Earth System Science, 124(6), pp.1311-1324.

Zangar, C.N., 1953. Theory and problems of water percolation (No. 8). Technical Information Office.

5 Appendix

Appendix A Civil Protection Identification of Flash Flood Susceptibility

Table A.1: Georeferences, translated English description, and classified flash flood susceptibility identified by local Civil Protection technicians.

NAME	LATITUDE	LONGITUDE	English Translation	Classified Susceptibility
Calle a Col Monsenor Romero	13.439903	-88.459446	In short storms of a couple of hours or minutes and in tropical storms	High
De la calle de cementerio de Santiago de María hacia La Claros	13.461559	-88.470936	Flash floods of one meter high that takes large rocks and causes danger to the population. Parents do not send their children to school out of fear.	High
Calle a San Mariano	13.431355	-88.449095	It is flooded by strong storms, collapsed street for the moment. Street to Santa Elena	High
Calle al desvio de California, El Saltillo	13.449770	-88.473948	In strong storms, the entire street is flooded by the union of the flash flood that drops from La Claros, Los Lunas and Col Regalo de Dios	High
Quebrada el Calvario	13.452826	-88.488660	Only when there are tropical storms or 55 mm and forward	Moderate
El Amate de El Jicaro	13.454407	-88.480500	It floods when there is a tropical storm, the parameters pass 50 mm	Moderate
Quebrada Los Angeles	13.458949	-88.493762	It floods when the parameters of the tropical storms pass 50 mm and isolats the community of Cerro Verde of Tecapan	Moderate

Rio Gualache, de el Calvario Tecapan	13.432665	-88.494797	It floods when the tropical storms pass 70 mm floods streets and homes	Low
Quebrada Sacatinta de Gualache, Tecapan	13.430156	-88.496580	It is flooded because the storm sewer does not have capacity with storms of more than 70 mm	Low
Quebrada El Playon de Gualache, Tecapan	13.430156	-88.496580	It floods when passes 70 mm	Low
Quebrada la Gallina de Comunidad El Bongo de Tecapan	13.428727	-88.498280	It floods with tropical storms of 50 mm of precipitation because it isolates communication between El Bongo and Gualache	Moderate
Quebrada de Arena de Loma Pacha de Los Chapetones, Tecapan	13.429184	-88.512477	It flooded in Hurricane Mitch in 1998 with precipitation of more than 100 mm and flooded homes	Low
Calle San Jose La Montanita	13.530364	-88.517066	The presence of rain in the municipality of Berlin generates flooding in the community of Montanita	High
Inundacion en el sector de la casa cumunal de San Jose La Mntanita	13.533691	-88.515842	The Communal House is identified for possible shelter despite being at a flood point	High
Calle principal del mercado municipal	13.483715	-88.467756	The street collapses due to heavy rains, also due to drainage problems	Moderate
Calle de Col Las Palmas	13.482776	-88.463823	The entire street is flooded due to the accumulation of small flash floods from different neighborhoods	Moderate
Quebrada de Colonia Guarumal	13.488326	-88.460428	The deep channel that joins waters east zone of the municipality	Moderate

Appendix B

B Google Earth Images, Drainage Dimension Estimates, and Bankfull Flow

Table B.1: Google Earth images, georeferences, estimated drainage dimensions, and bankfull flow.

Image Number	Georeference (Decimal Degrees)	Drainge Dimensions (m)	Bankfull Flow Estimate (Manning's Equation) (m^3/s)
DW1	13.455080°, -88.471200°	Width: 2 Height: 1	3.60
DW2	13.454930°, -88.471370°	Width: 2 Height: 1	3.60
DW3	13.454880°, -88.471430°	Width: 2 Height: 1	3.60
DW4	13.454640°, -88.472000°	Width: 6 Height: 3	67.39
DW5	13.454680°, -88.472030°	Width: 6 Height: 3	67.39
DW6	13.454522°, -88.472222°	Width: 6 Height: 3	67.39
DW7	13.454564°, -88.472364°	Width: 6 Height: 3	67.39
DW8	13.453590°, -88.473200°	Width: 6 Height: 3	67.39
DW9	13.453542°, -88.473200°	Width: 6 Height: 3	67.39
DW10	13.449628°, -88.474589°	Width: 6 Height: 3	67.39
DW11	13.449590°, -88.474730°	Width: 6 Height: 3	67.39
DW12	13.449580°, -88.474740°	Width: 6 Height: 3	67.39
DW13	13.448460°, -88.474980°	Width: 2 Height: 1	3.60
DW14	13.446950°, -88.475230°	Width: 2 Height: 1	3.60
DW15	13.443950°, -88.476860°	Width: 2 Height: 1	3.60
DW16	13.443840°, -88.476810°	Width: 2 Height: 1	3.60
DW17	13.443790°, -88.476940°	End of drainage (road)	

Bankfull flow is the maximum discharge (m^3/s) a stream channel can carry before overflowing (Oxford reference, 2023). The bankfull flow of the La Claros drainage at each Google Earth point (Appendix B Table B.1) is estimated using Manning's equation below (Normal depth calculator).

Manning's Bankfull Flow

$$Q = \frac{AR^{2/3}S^{1/2}}{n}$$

Q = Flow Rate, (m^3/s)
A = Flow area, (m^2)
R = Hydraulic radius, (m)
S = Channel slope
n = Manning's roughness coefficient

Flow area (A) is determined using the estimated widths and heights at various locations along the La Claros drainage (Appendix B Table B.1). Hydraulic radius (R) is the Area/Wetted perimeter. The Wetted perimeter is the width+2*height. Channel slope is taken from Figure 16 which shows the Google Earth La Claros drainage walk elevation profile and average slope (0.01). Using images from the drainage walk (Figure 17), Manning's roughness coefficient is estimated as 0.035 which describes the main channel as "clean, straight, full stage, no rifts or deep pools, more stones, and weeds" (Manning's n values, 2006). Using Manning's equation, where the channel width is 2 meters and depth is 1 meter, the bankfull flow is calculated to be 3.60 m^3/s. Where the channel width is 6 meters wide and 3 meters deep, the bankfull flow is estimated as 67.39 m^3/s (Appendix B Table B.1). These values are the maximum streamflow rate if the channel was flowing full.

Appendix C

C ArcGIS Pro Catchment Area, Tributary Length and Slope

Table C.1: Catchment area, runoff resistance factor, tributary length, and tributary slope.

Tributary	Catchment Shape Area (km^2)	Runoff Resistance Factor	Tailflow Point (Tributary Length) (km)	Preferred Flow Direction (Tributary slope)
Tributary 1	1.61	3.50	2.34	0.16
Tributary 2	0.61	2.50	0.76	0.04
Tributary 3	1.13	3.50	2.03	0.12
Tributary 4	0.6	3.75	2.15	0.05
Tributary 5	0.9	3.50	0.96	0.03
Tributary 6	1.34	3.50	0.80	0.07
Tributary 7	1.1	3.50	0.94	0.08
Tributary 8	1.19	3.75	3.36	0.13
Tributary 9	0.55	3.50	0.78	0.04
Tributary 10	1.01	3.50	1.23	0.06
Tributary 11	1.56	3.75	2.23	0.26
Tributary 12	2.42	3.50	2.79	0.19
Tributary 13	1.48	3.75	1.91	0.13
Tributary 14	1.14	2.50	2.27	0.06
Tributary 15/15_2	2.27	2.00	3.65	0.07
Tributary 16	3.59	3.75	3.82	0.13
Tributary 17	1.66	3.50	1.62	0.23
Tributary 18	0.77	3.50	0.64	0.04

Appendix D

D Infiltrometer Data for Site BH

Table D.1: Data for site BH1.

Site: **BH1**	
Latitude	13.45637
Longitude	-88.47024
Depth of borehole (cm)	38.4
Depth to water (cm)	23
Height of water in borehole, *H* (cm)	20.4
Diameter of borehole, *D (*cm)	7.4
Average Flow at SS, *Q* (ml/min)	66
Saturated Hydraulic Conductivity, *Ksat* (cm/min)	0.015

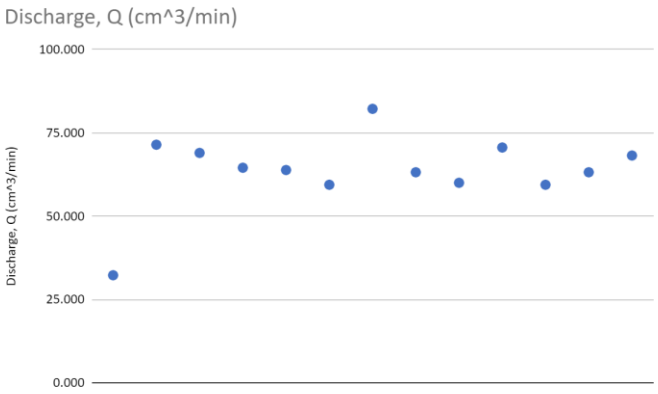

Observed Volume (cc)	**Delta *t* (sec)**	**Delta *t* (min)**	**Water Volume (cm^3)**	**Discharge, *Q* (cm^3/min)**
0				
200	186	3.10	100	32.258
300	84	1.40	100	71.429
400	87	1.45	100	68.966
500	93	1.55	100	64.516
600	94	1.57	100	63.830
700	101	1.68	100	59.406
800	73	1.22	100	82.192
900	95	1.58	100	63.158
1000	100	1.67	100	60.000
1100	85	1.42	100	70.588
1200	101	1.68	100	59.406
1300	95	1.58	100	63.158
1400	88	1.47	100	68.182

Table D.2: Data for site BH2.

Site: **BH2**	
Latitude	13.45637
Longitude	-88.47024
Depth of borehole (cm)	35
Depth to water (cm)	19
Height of water in borehole, *H* (cm)	20
Diameter of borehole, *D* (cm)	6.5
Average Flow at SS, *Q* (ml/min)	185
Saturated Hydraulic Conductivity, *Ksat* (cm/min)	0.044

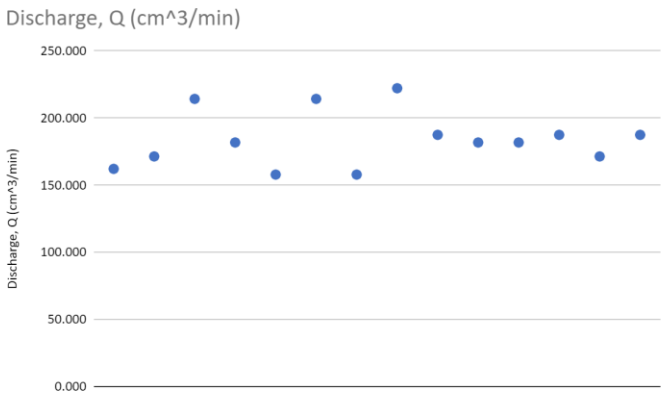

Observed Volume (cc)	**Delta *t* (sec)**	**Delta *t* (min)**	**Water Volume (cm^3)**	**Discharge, *Q* (cm^3/min)**
0				
100	37	0.62	100	162.162
200	35	0.58	100	171.429
300	28	0.47	100	214.286
400	33	0.55	100	181.818
500	38	0.63	100	157.895
600	28	0.47	100	214.286
700	38	0.63	100	157.895
800	27	0.45	100	222.222
900	32	0.53	100	187.500
1000	33	0.55	100	181.818
1100	33	0.55	100	181.818
1200	32	0.53	100	187.500
1300	35	0.58	100	171.429
1400	32	0.53	100	187.500

Table D.3: Data for site BH3.

Site: **BH3**	
Latitude	13.45637
Longitude	-88.47024
Depth of borehole (cm)	37
Depth to water (cm)	19
Height of water in borehole, *H* (cm)	20
Diameter of borehole, *D* (cm)	6.3
Average Flow at SS, *Q* (ml/min)	98
Saturated Hydraulic Conductivity, *Ksat* (cm/min)	0.023

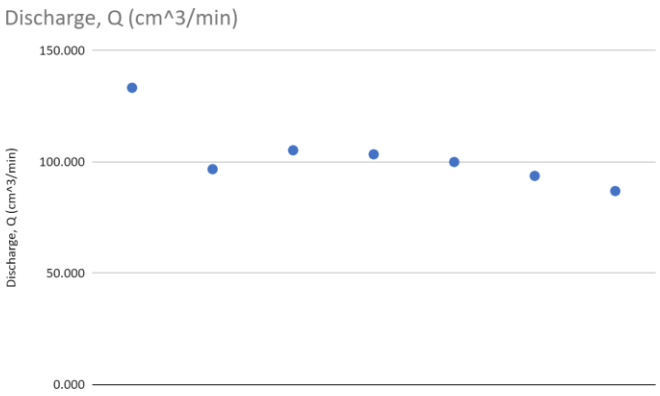

Observed Volume (cc)	**Delta *t* (sec)**	**Delta *t* (min)**	**Water Volume (cm^3)**	**Discharge, *Q* (cm^3/min)**
1300				
1400	45	0.75	100	133.333
1500	62	1.03	100	96.774
1600	57	0.95	100	105.263
1700	58	0.97	100	103.448
1800	60	1.00	100	100.000
1900	64	1.07	100	93.750
2000	69	1.15	100	86.957

Appendix E

E Infiltrometer Data for Site LC

Table E.1: Data for site LC1.

Site: **LC1**	
Latitude	13.45747
Longitude	-88.47204
Depth of borehole (cm)	33.4
Depth to water (cm)	20
Height of water in borehole, *H* (cm)	20
Diameter of borehole, *D* (cm)	6.5
Average Flow at SS, *Q* (ml/min)	70
Saturated Hydraulic Conductivity, *Ksat* (cm/min)	0.017

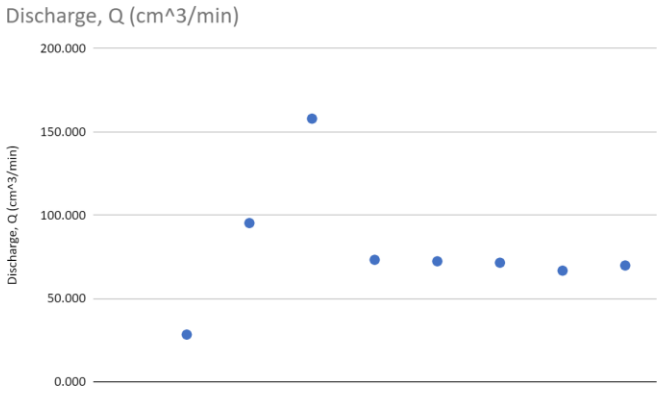

Observed Volume (cc)	**Delta *t* (sec)**	**Delta *t* (min)**	**Water Volume (cm^3)**	**Discharge, *Q* (cm^3/min)**
200				
300	212	3.53	100	28.302
400	63	1.05	100	95.238
500	38	0.63	100	157.895
600	82	1.37	100	73.171
700	83	1.38	100	72.289
800	84	1.40	100	71.429
900	90	1.50	100	66.667
1000	86	1.43	100	69.767
1100	89	1.48	100	67.416

Table E.2: Data for site LC2.

Site: **LC2**	
Latitude	13.45747
Longitude	-88.47204
Depth of borehole (cm)	36
Depth to water (cm)	17
Height of water in borehole, *H* (cm)	20
Diameter of borehole, *D* (cm)	6
Average Flow at SS, *Q* (ml/min)	60
Saturated Hydraulic Conductivity, *Ksat* (cm/min)	0.014

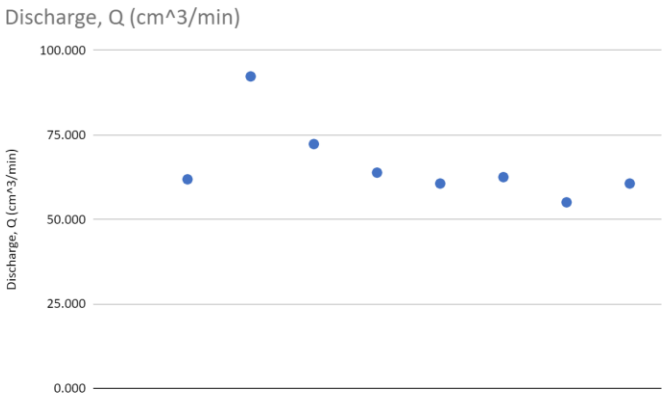

Observed Volume (cc)	**Delta *t* (sec)**	**Delta *t* (min)**	**Water Volume (cm^3)**	**Discharge, *Q* (cm^3/min)**
200				
300	97	1.62	100	61.856
400	65	1.08	100	92.308
500	83	1.38	100	72.289
600	94	1.57	100	63.830
700	99	1.65	100	60.606
800	96	1.60	100	62.500
900	109	1.82	100	55.046
1000	99	1.65	100	60.606
1100	104	1.73	100	57.692

Table E.3: Data for site LC3.

Site: **LC3**	
Latitude	13.45747
Longitude	-88.47204
Depth of borehole (cm)	33
Depth to water (cm)	25
Height of water in borehole, *H* (cm)	20
Diameter of borehole, *D* (cm)	6.5
Average Flow at SS, *Q* (ml/min)	48
Saturated Hydraulic Conductivity, *Ksat* (cm/min)	0.011

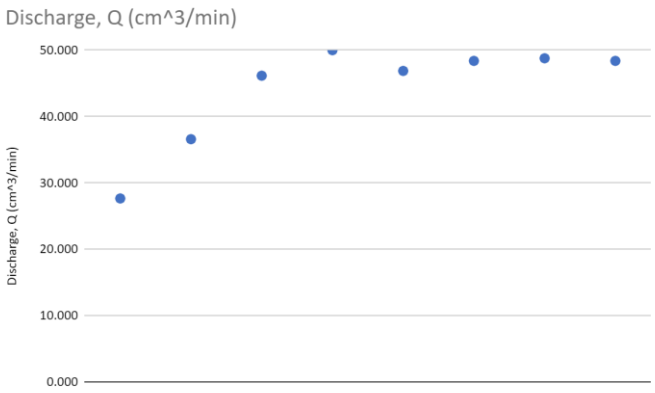

Observed Volume (cc)	**Delta *t* (sec)**	**Delta *t* (min)**	**Water Volume (cm^3)**	**Discharge, *Q* (cm^3/min)**
0				
100	217	3.62	100	27.650
200	164	2.73	100	36.585
300	130	2.17	100	46.154
400	120	2.00	100	50.000
500	128	2.13	100	46.875
600	124	2.07	100	48.387
700	123	2.05	100	48.780
800	124	2.07	100	48.387

Appendix F

F Infiltrometer Data for Site LL

Table F.1: Data for site LL1.

Site: **LL1**	
Latitude	13.47215
Longitude	-88.47429
Depth of borehole (cm)	34
Depth to water (cm)	22
Height of water in borehole, *H* (cm)	20
Diameter of borehole, *D* (cm)	6.5
Average Flow at SS, *Q* (ml/min)	106
Saturated Hydraulic Conductivity, *Ksat* (cm/min)	0.025

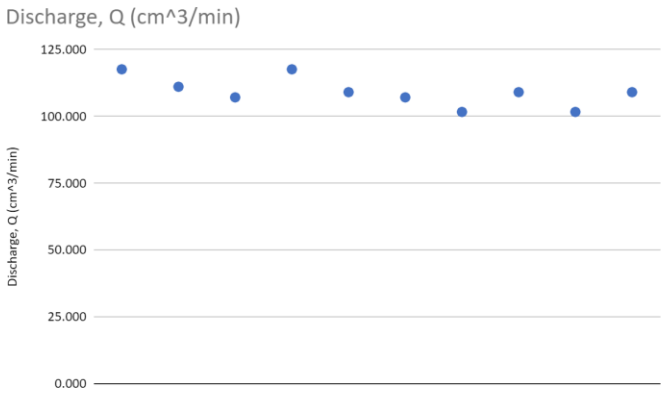

Observed Volume (cc)	**Delta *t* (sec)**	**Delta *t* (min)**	**Water Volume (cm^3)**	**Discharge, *Q* (cm^3/min)**
100				
200	51	0.85	100	117.647
300	54	0.90	100	111.111
400	56	0.93	100	107.143
500	51	0.85	100	117.647
600	55	0.92	100	109.091
700	56	0.93	100	107.143
800	59	0.98	100	101.695
900	55	0.92	100	109.091
1000	59	0.98	100	101.695
1100	55	0.92	100	109.091

Table F.2: Data for site LL2.

Site: **LL2**	
Latitude	13.47215
Longitude	-88.47429
Depth of borehole (cm)	36
Depth to water (cm)	22
Height of water in borehole, *H* (cm)	20
Diameter of borehole, *D* (cm)	6.4
Average Flow at SS, *Q* (ml/min)	76
Saturated Hydraulic Conductivity, *Ksat* (cm/min)	0.018

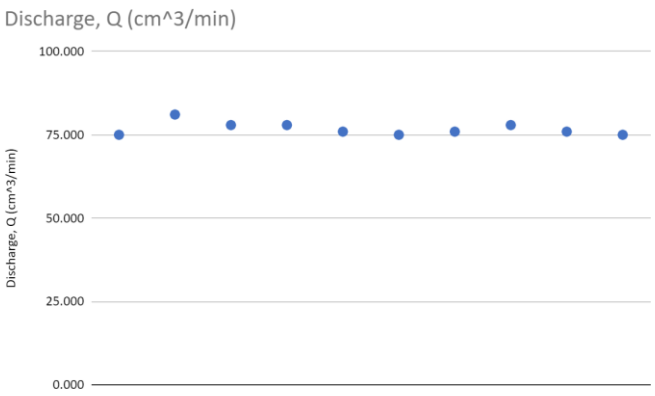

Observed Volume (cc)	**Delta *t* (sec)**	**Delta *t* (min)**	**Water Volume (cm^3)**	**Discharge, *Q* (cm^3/min)**
0				
100	80	1.33	100	75.000
200	74	1.23	100	81.081
300	77	1.28	100	77.922
400	77	1.28	100	77.922
500	79	1.32	100	75.949
600	80	1.33	100	75.000
700	79	1.32	100	75.949
800	77	1.28	100	77.922
900	79	1.32	100	75.949
1000	80	1.33	100	75.000

Table F.3: Data for site LL3.

Site: **LL3**	
Latitude	13.47215
Longitude	-88.47429
Depth of borehole (cm)	32
Depth to water (cm)	15
Height of water in borehole, *H* (cm)	20
Diameter of borehole, *D* (cm)	6
Average Flow at SS, *Q* (ml/min)	103
Saturated Hydraulic Conductivity, *Ksat* (cm/min)	0.026

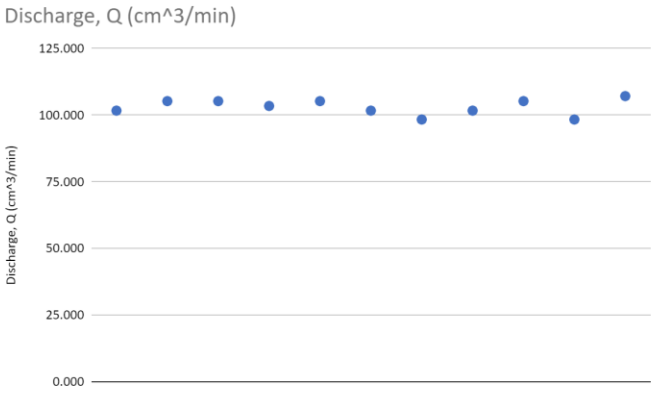

Observed Volume (cc)	**Delta *t* (sec)**	**Delta *t* (min)**	**Water Volume (cm^3)**	**Discharge, *Q* (cm^3/min)**
300				
400	59	0.98	100	101.695
500	57	0.95	100	105.263
600	57	0.95	100	105.263
700	58	0.97	100	103.448
800	57	0.95	100	105.263
900	59	0.98	100	101.695
1000	61	1.02	100	98.361
1100	59	0.98	100	101.695
1200	57	0.95	100	105.263
1300	61	1.02	100	98.361
1400	56	0.93	100	107.143